https://doi.org/10.5194/egusphere-2026-4897
Preprint. Discussion started: 31 August 2026

Characterizing snow grain size and shape evolution across 20 scenarios of dry snow metamorphism

Oscar Dick[1], Neige Calonne[1], and Pascal Hagenmuller[1]

[1]Météo-France, CNRS, Univ. Grenoble Alpes, Univ. Toulouse, CNRM, Centre d'Études de la Neige, 38000 Grenoble, France

Correspondence: Oscar Dick (oscar.dick@meteo.fr)

Abstract.

Snow microstructure evolves continuously during dry snow metamorphism, governing many effective physical properties of snow. Accurately representing this evolution in snowpack models requires objective descriptors of grain size and grain shape together with reliable temporal evolution laws. However, the evolution of snow microstructure has not been systematically characterized over the full range of dry snow metamorphism conditions. Here, we investigate the temporal evolution of several grain-size and grain-shape descriptors during dry snow metamorphism using a unique 4D X-ray tomography dataset comprising 20 experiments covering a broad range of temperatures, temperature gradients, and initial snow types. We analyze specific surface area (SSA), optical and microwave grain sizes, correlation length, structural anisotropy, three curvature-based grain-shape descriptors, as well as the full chord length and mean curvature distributions. Our results reveal that SSA evolution is far more diverse than generally assumed, including transient increases under strong temperature gradients. Optical and microwave grain-size descriptors often differ in both absolute value and temporal evolution, suggesting that snowpack models should predict both rather than a single grain-size descriptor. Vertical structural anisotropy does not systematically develop under temperature gradients, contrary to the common assumption. Overall, the initial snow microstructure strongly controls grain-shape evolution and, to a lesser extent, grain-size evolution, while both are also influenced by temperature gradient and mean temperature. These results provide new experimental constraints for developing and evaluating snow microstructure representations and temporal evolution laws in snowpack models. Future snowpack models could benefit from predicting the full chord length and mean curvature distributions rather than only scalar descriptors.

1 Introduction

Dry snow microstructure consists of an arrangement of sintered ice crystals surrounded by air. This microstructure evolves due to thermodynamic disequilibrium at the ice-air interfaces, known as dry snow metamorphism (Yosida et al., 1955; Colbeck, 1983). Two types of transformations are classically distinguished in dry snow metamorphism: equi-temperature metamorphism (ETM) and temperature-gradient metamorphism (TGM). These transformations

https://doi.org/10.5194/egusphere-2026-4897
Preprint. Discussion started: 31 August 2026

generate a wide diversity of snow microstructures characterized by grains of different sizes and shapes (e.g., Fierz et al., 2009). Characterizing snow microstructure and its evolution during metamorphism is essential for many snow-related applications, as snow microstructure controls snowpack behavior at larger scales, such as avalanche release (e.g., Schweizer et al., 2003), hydrology of mountain regions (e.g., Holko et al., 2011), and Earth's surface energy budget (e.g., Dumont et al., 2014).

Snow microstructure has traditionally been described in terms of grain size and grain shape. In field observations, these quantities are assessed visually following the International Classification for Seasonal Snow on the Ground (Colbeck et al., 1990; Fierz et al., 2009). After manually separating the grains, grain size is defined as the largest extension of a grain and grain shape is described qualitatively through the snow type. Detailed snowpack models, such as CROCUS and SNOWPACK (Lafaysse et al., 2025; Lehning et al., 2002), naturally adopt this framework by representing snow microstructure through grain size and grain shape. Grain size is represented by the optical grain diameter derived from the specific surface area (SSA), whereas grain shape is characterized by an empirical sphericity index.

Although this representation has proved successful in many applications, it has several limitations. The empirical sphericity index cannot be measured, preventing quantitative comparisons with experiments and making it difficult to relate directly to the physical properties of snow. The temporal evolution of SSA is described by empirical laws. Recent studies have shown that these laws do not always reproduce field observations under alpine and Arctic conditions (e.g., Morin et al., 2013; Barrere et al., 2017; Domine et al., 2019; Calonne et al., 2020; Woolley et al., 2024, 2026). In addition, these two quantities do not necessarily capture all the microstructural information required to model certain effective properties, such as thermal conductivity (e.g., Calonne et al., 2014b) or microwave radiative properties (e.g., Picard et al., 2022). Addressing these limitations first requires identifying objective descriptors of grain size and grain shape.

More generally, describing the size and shape of the skeletal portion composing a porous medium has been a long-standing issue (Torquato, 2002). Notions of size and shape are intertwined, and it can be complicated or even meaningless to disentangle them. Various geometrical descriptors have therefore been developed to characterize porous media. Among the most widely used are the Minkowski functionals, the chord length distribution, and the two-point correlation (or autocorrelation) function (Torquato, 2002). For a 3D space, the Minkowski functionals comprise the total volume, surface area, integral mean curvature, and integral Gaussian curvature. Together, they provide a compact (and complete, under certain conditions) description of the geometry and topology of porous media, as established by Hadwiger's theorem (Hadwiger, 1957). The chord length distribution characterizes the lengths of linear segments contained within a given phase of the porous medium and has proved useful for transport phenomena, such as Knudsen diffusion and radiative transfer (Ho and Strieder, 1979; Tassopoulos and Rosner, 1992). The two-point correlation function characterizes spatial correlations within the microstructure, from which characteristic structural length scales can be derived (Torquato, 2002).

https://doi.org/10.5194/egusphere-2026-4897
Preprint. Discussion started: 31 August 2026

When it comes to describing snow microstructure, the choice of the pertinent geometrical descriptor depends on the physical process of interest. For example, the size and shape of the snow grains that a photon experiences in the visible light range are not the same as in the microwave range. In the following, we present commonly used geometrical parameters that can be defined unambiguously and that are or could be related to snow effective physical properties. Specific surface area (SSA) describes the ratio between the total surface area and the total snow mass or volume (e.g., Arakawa et al., 2009). This property is of primary importance for radiative transfer in the visible and near-infrared ranges, as it is directly related to snow albedo (Wiscombe and Warren, 1980; Gardner and Sharp, 2010; Dumont et al., 2017). The optical grain size, also referred to as the spherical equivalent grain size, can be directly derived from SSA (Warren, 1982; Grenfell et al., 1994). Curvature characterizes the local shape of the ice-air interface (Coléou et al., 2001; Flin et al., 2004; Calonne et al., 2014a). It is of particular interest for dry snow metamorphism because curvature gradients drive vapor transport and therefore the evolution of the snow microstructure. The variance of mean curvature quantifies the geometrical heterogeneity of the ice surface and has recently been proposed as a controlling factor for SSA evolution (Braun et al., 2024). The first moment of the chord length distribution is related to SSA (Underwood, 1969), whereas higher-order moments contain additional information on the distribution of structural length scales and can be related to the optical and microwave radiative properties of snow (Malinka, 2014). Recently, a microwave grain size, based on the moments of the chord length distribution, was introduced by Picard et al. (2022) to model microwave scattering by the snowpack. Different characteristic lengths can be derived from the two-point or autocorrelation function (Mätzler, 2002), including the exponential correlation length (Löwe et al., 2013; Calonne et al., 2014a; Krol and Löwe, 2016), which is strongly related to microwave radiative transfer in snow (Vallese and Kong, 1981; Wiesmann and Mätzler, 1999). The structural anisotropy of snow describes the preferential orientation of the snow microstructure. It can be computed from any directional geometrical property, but is often calculated with the correlation lengths (e.g., Löwe et al., 2013; Calonne et al., 2014a; Leinss et al., 2020). It governs the anisotropy of several physical properties of snow, such as thermal conductivity, diffusivity, or electromagnetic permittivity (e.g., Calonne et al., 2012, 2014b; Leinss et al., 2020; Sundu et al., 2024). Finally, the Euler characteristic and the genus are topological invariants which have been used to describe the connectivity, or bond network, within the microstructure (e.g., Schleef et al., 2014a; Hagenmuller et al., 2014; Bernard et al., 2023).

The influence of metamorphism conditions on the above-mentioned geometrical metrics has been investigated only for a limited number of cases. Most studies are based on cold-laboratory experiments and X-ray tomography. Concerning SSA, while a decrease with time is commonly observed (e.g., Flin et al., 2003; Schneebeli and Sokratov, 2004; Taillandier et al., 2007; Kaempfer and Schneebeli, 2007; Hachikubo et al., 2014; Wiese and Schneebeli, 2017), different evolutions, such as an increase in SSA, have been reported for specific conditions (Domine et al., 2009; Wang and Baker, 2014; Bouvet et al., 2023) but remain to be more thoroughly characterized. The exponential correlation lengths (e.g., Löwe et al., 2013; Schleef and Loewe, 2013; Calonne et al., 2014a), curvature distributions (e.g., Coléou et al., 2001; Flin et al., 2004; Calonne et al., 2014a), and the anisotropy of the exponential length (e.g., Löwe et al., 2013; Calonne et al., 2014a; Leinss et al., 2016) have been studied only for a few specific cases of

https://doi.org/10.5194/egusphere-2026-4897
Preprint. Discussion started: 31 August 2026

metamorphism, which prevents a comprehensive picture of their evolution from being drawn. Regarding structural anisotropy, a simple model of its temporal evolution was proposed by Leinss et al. (2020) as an attempt to enable the use of the anisotropy in snowpack models as an internal variable. This model was evaluated on five cases of dry snow metamorphism due to the lack of additional suitable data. More recently, Braun et al. (2024) proposed a physically based evolution law for SSA. Although promising, this model still requires some empirical adjustments and has not yet been thoroughly evaluated because of the lack of experimental datasets covering a sufficiently broad range of dry snow metamorphism conditions. These studies highlight the need for a more systematic characterization of the evolution of grain-size and grain-shape descriptors across the broad range of dry snow metamorphism conditions encountered in nature. Such observational data are needed both to improve the physical understanding of snow metamorphism and to develop and evaluate temporal evolution laws for snowpack models.

Here, we provide the first systematic characterization of the temporal evolution of multiple grain-size and grain-shape descriptors across a broad range of dry snow metamorphism conditions using the 4D dataset of Dick et al. (2026b). It consists of time series of 3D tomographic images from 20 snow metamorphism experiments with systematic variations of temperature gradient, temperature, and initial snow microstructure. We focus on objectively measurable metrics of potential interest for the modeling of the snow microstructure and its physical properties. We investigate the temporal evolution of SSA, the distribution of chord lengths and its derived microwave grain size, the distribution of surface mean curvature and its variance, and the exponential correlation length and its anisotropy ratio. In addition, we investigate two complementary descriptors of grain shape and topology: the Willmore energy and the genus. The Willmore energy, derived from the mean and Gaussian curvatures, quantifies how much a surface deviates from a spherical or planar shape (Willmore, 1992), while the genus is a topological descriptor closely related to the Euler characteristic that describes the connectivity of grains within the porous medium (Richeson, 2010; Schleef et al., 2014c).

The paper is organized as follows. Section 2 presents the experimental dataset together with the definitions and methods used to characterize grain size and shape. Section 3 describes the temporal evolution of the grain size and grain shape descriptors, followed in Section 4 by their analysis and implications for snowpack modeling.

2 Method

2.1 4D tomographic dataset

This study is based on the experimental dataset of Dick et al. (2026b), which consists of 20 time series of 3D tomographic images of snow evolving under various dry snow metamorphism scenarios. The experiments cover a subset of the combinations of three mean temperatures (-3, -8, and -17°C) with four temperature gradients (0, 10, 40, and 100 K m^{-1}), applied to five initial snow types defined as follows:

https://doi.org/10.5194/egusphere-2026-4897
Preprint. Discussion started: 31 August 2026

- The DF samples refer to 5 samples of decomposing and fragmented precipitation particles with rimed surfaces (towards graupel), with densities between 84 and 91 kg m^{-3} and SSA values between 57 and 58 m^2 kg^{-1}.
- The RGl samples refer to 10 samples of rounded grains considered as light in the present study, with densities between 225 and 245 kg m^{-3} and SSA values between 27 and 28 m^2 kg^{-1}.
- The RGd samples refer to 3 samples of rounded grains considered as dense, with densities between 335 and 345 kg m^{-3} and SSA values between 19 and 20 m^2 kg^{-1}.
- The FC sample refers to 1 sample of faceted crystals of density 243 kg m^{-3} and of SSA 23 m^2 kg^{-1}.
- The DH sample refers to 1 sample of depth hoar of density 225 kg m^{-3} and of SSA 21 m^2 kg^{-1}.

The temporal evolution of each snow sample was monitored for 7 days, with scans acquired every 4 hours at a nominal voxel size of 8.45 μm. The tomograph was located in a cold laboratory, and the thermal conditions around the snow samples were controlled by a dedicated environmental cell installed inside the tomograph. The images have a size of length × width × height = 11 × 11 × 7.6 mm^3. This volume is sufficiently large to be representative of the whole snow sample under study (Kaempfer et al., 2005; Brzoska et al., 2008; Zermatten et al., 2011; Calonne et al., 2011). For all the experiments, an ice layer was prepared at the bottom of the snow sample to avoid the formation of an air gap, which would alter the temperature gradient. For 12 time series, the bottom ice layer appears on the images and was cropped before calculation. The maximum cropped height was 0.4 mm. The snow within the volume is homogeneous, which has been assessed both qualitatively and quantitatively. In the Appendix, Figure A1 shows the homogeneity of the vertical profiles of SSA and density for RGl samples exposed to three temperature gradients at -3°C. Snow density remains nearly constant throughout the experiments. Only the DF samples exhibit a small increase of 5–10 kg m^{-3} over the 7-day experiments (Appendix, Figure A2). A full description of the experimental setup is provided by Dick et al. (2026b), and the complete 4D dataset is available in Dick et al. (2026a). Videos of the 20 snow evolution time series are available on YouTube at https://www.youtube.com/@Snow-Science.

2.2 Computation of the grain size and shape descriptors

Specific surface area and optical diameter

Specific surface area of snow (SSA, in m^2 kg^{-1}) is the total ice surface area per unit snow mass. A characteristic grain size for optical applications, the optical diameter (Warren, 1982), is derived from SSA as

$$d_{\mathrm{opt}} = \frac{6}{\mathrm{SSA}\rho_{\mathrm{ice}}} \qquad (1)$$

with ρ_{ice} the ice density equal to 917.5 kg m^{-3}. The optical diameter corresponds to the diameter of a sphere having the same SSA as the considered snow volume.

https://doi.org/10.5194/egusphere-2026-4897
Preprint. Discussion started: 31 August 2026

In this study, SSA was calculated using the Crofton approach described in Lehmann and Legland (2012) with a 26-neighbor adjacency. This method is based on the Cauchy-Crofton formula, which explicitly relates the surface area to the number of intersections with any straight line in a 3D volume (Boykov and Kolmogorov, 2003). Its high accuracy compared to other area computation methods for various images was demonstrated by Hagenmuller et al. (2016). Optical diameter was derived from SSA using Eq. (1).

Chord length distribution

The chord length distribution $p(l)$ describes the probability of finding chords of a specific length l in the microstructure. It characterizes the full spectrum of structural length scales within the ice matrix. The first moment of the distribution, i.e., the mean chord length, is related to the optical diameter (Underwood, 1969), while the full distribution can be used to derive all optical properties of the microstructure (Malinka, 2014) and is linked to the two-point correlation function (Méring and Tchoubar, 1968) under certain assumptions discussed in Krol and Löwe (2016).

The chord length distribution of the ice phase was computed from the 3D tomographic images in each Cartesian direction x, y, and z of the snow volume, and the lengths of intersections between these lines and the ice phase are called chord lengths (l). Chords intersecting the image boundaries were discarded. The chord length distributions obtained along the three Cartesian directions are denoted by $p(l_x)$, $p(l_y)$, and $p(l_z)$.

Microwave grain size

The microwave grain size (l_{MW}, in mm) was introduced by Picard et al. (2022) as a grain size metric that optimally describes microwave scattering by snow. It is defined as the Porod length l_p weighted by a factor K called polydispersity, as:

$$l_{MW} = K l_p \tag{2}$$

The Porod length l_p is the inverse of the slope at the origin of the autocorrelation of the indicator function (Debye et al., 1957), and is linked to the SSA and density ρ of snow through (Krol and Löwe, 2016; Picard et al., 2022):

$$l_p = 4\frac{1-\phi}{\mathrm{SSA}\rho_{\mathrm{ice}}} \tag{3}$$

with $\phi = \rho/\rho_{\mathrm{ice}}$ the volume fraction of ice, ρ being the snow density, and ρ_{ice} the ice density.

The polydispersity factor K characterizes how widely the length scales vary within the microstructure and carries information on the shape and relative arrangement of the grains, as described in Picard et al. (2022). This factor depends on ratios of the first four moments of the chord length distribution, as:

$$K = \left(\frac{\mu_4}{24\mu_1^4} - \frac{\mu_2\mu_3}{6\mu_1^5}\phi + \frac{\mu_2^3}{8\mu_1^6}\phi^2\right)(1-\phi)^{-2/3} \tag{4}$$

https://doi.org/10.5194/egusphere-2026-4897
Preprint. Discussion started: 31 August 2026

where μ_1, μ_2, μ_3, μ_4 are the first four moments of the chord length distribution. In the present work, the i-th moment was computed by combining the chord length distributions measured along the three Cartesian directions as:

$$\mu_i = \frac{1}{3} \sum_{j \in \{x,y,z\}} \int_l l_j^i p(l_j)\, dl \tag{5}$$

where j denotes the Cartesian direction and $p(l_j)$ is the probability of observing a chord of length l in direction j.

Exponential correlation length

The exponential correlation length (l_c, in mm) is a characteristic length of the snow microstructure derived from the two-point correlation (or autocorrelation) function of the indicator function (Debye et al., 1957; Torquato, 2002). The two-point correlation function is defined as:

$$C(r_i) = \overline{I(x+r_i)I(x)} - \phi^2 \tag{6}$$

with the ice phase indicator function $I(x)$, which is equal to 1 in the ice and 0 in the air, r_i the displacement in the Cartesian direction $i = x, y, z$, and ϕ the volume fraction of ice. In snow, the two-point correlation function decreases approximately exponentially with r_i, and the decay rate depends on the size and arrangement of the microstructure. Different characteristic lengths can be derived from the two-point correlation function, as described in Mätzler (2002). The slope of the two-point correlation function at the origin can be expressed in terms of SSA (Debye et al., 1957), while the third derivative of the function at the origin can be related to the curvature length (Krol and Löwe, 2016). Here we used the approach based on an exponential fit (e.g., Mätzler, 2002; Löwe et al., 2013; Calonne et al., 2014a; Krol and Löwe, 2016), in which a length, called exponential correlation length, l_{c_i} is derived by fitting the normalized two-point correlation function in the Cartesian direction i with an exponential function of the form:

$$\frac{C(r_i)}{C(0)} = \exp\left(\frac{-r_i}{l_{c_i}}\right) \tag{7}$$

In porous media, the vector $(l_{c_x}, l_{c_y}, l_{c_z})$ is often used as a characteristic length scale of the microstructure, without distinguishing between the ice and pore phases (Calonne, 2014).

In this study, we computed the two-point correlation function from the tomographic images using the Fast Fourier Transform (e.g., Newman and Barkema, 1999) in each Cartesian spatial direction x, y, and z. In practice, displacements r_i up to half the image size were considered for each Cartesian direction (i.e., 5.5 mm for directions x and y and 3.8 mm for direction z minus the cropped ice layer when applicable). The exponential correlation lengths l_{c_x}, l_{c_y}, and l_{c_z} were then derived by applying Eq. (7) to each obtained two-point correlation function. The fit was made using a least-squares approximation on the full displacement range r_i for each Cartesian direction i. An example of a two-point correlation function and its exponential fit is provided in the Appendix (Figure A3). An average exponential correlation length l_c was computed as the arithmetic mean of the three lengths:

$$l_c = \frac{l_{c_x} + l_{c_y} + l_{c_z}}{3} \tag{8}$$

https://doi.org/10.5194/egusphere-2026-4897
Preprint. Discussion started: 31 August 2026

Note that this metric is called exponential correlation length in Mätzler (2002) and Krol and Löwe (2016), in reference to the exponential fit applied, but, for the sake of conciseness, is simply called correlation length in this study.

Structural anisotropy

The structural anisotropy A characterizes the preferential orientation of the ice matrix, i.e., its elongation along a particular spatial direction. It can be derived from any length defined in the three Cartesian directions, but it is often calculated based on the anisotropy of the correlation lengths (Löwe et al., 2013; Calonne et al., 2014a; Leinss et al., 2020) and defined as:

$$A(l_c) = \frac{2l_{c_z}}{l_{c_x} + l_{c_y}} \tag{9}$$

where $l_{c_x}, l_{c_y}, l_{c_z}$ are the correlation lengths in the directions x, y, and z, as described above. The ice matrix of snow is isotropic when $A(l_c) = 1$, is anisotropic and preferentially elongated along the vertical axis when $A(l_c) > 1$, and is anisotropic and preferentially elongated along the horizontal plane when $A(l_c) < 1$. Another definition of structural anisotropy has been proposed by Leinss et al. (2016), as the relative difference of the correlation lengths between the horizontal and vertical axes. However, both definitions are related as shown in Leinss et al. (2020). We calculated the correlation length in each Cartesian direction using the method described in the paragraph above, and the structural anisotropy using Eq. (9).

Surface curvature distribution

At a given point of the 3D image on the ice-air interface, two principal curvatures can be calculated: a maximum curvature κ_1 and a minimum curvature κ_2. From these two curvatures, mean curvature H and Gaussian curvature K can be calculated as:

$$\begin{cases} H &= \frac{1}{2}(\kappa_1 + \kappa_2) \\ K &= \kappa_1 \kappa_2 \end{cases} \tag{10}$$

In the present work, the normal vector field at the ice-air interface is oriented from ice to air, which translates into a convex or saddle-shaped surface for $H > 0$, a concave or saddle-shaped surface for $H < 0$, and a flat surface for $H = 0$.

Mean and Gaussian curvatures were computed from the 3D images using the open-source library DGtal (DGtal). This library calculates curvatures on discrete surfaces using a numerically efficient method based on the theoretical work of Lachaud et al. (2022). Curvature was calculated using the Interpolated Corrected Normal Current (ICNC) method. The radius to compute the ICNC curvature was set to 4 voxels, while the ring radius to compute the convolved normal was set to 3 voxels. We regularized the surface before computing the curvature, and discarded the voxels in the vicinity of the image borders (a 5-voxel, or 0.04 mm, margin was taken at each border).

https://doi.org/10.5194/egusphere-2026-4897
Preprint. Discussion started: 31 August 2026

Mean curvature variance

The mean curvature variance (σ_H^2, in mm^{-2}) describes the dispersion of the local mean curvature values around the average mean curvature. It is zero for a collection of spheres of identical size, while it is positive for spheres with different sizes or with surface irregularities. Thus, it can be interpreted as a descriptor of the irregularities of grain surface or heterogeneity of grain size. The mean curvature variance appears as a driving term in the SSA evolution law proposed by Braun et al. (2024). The mean curvature variance is defined as:

$$\sigma_H^2 = \frac{1}{S}\int_S H^2\,ds - \left(\frac{1}{S}\int_S H\,ds\right)^2 \tag{11}$$

We derived the mean curvature variance from the mean curvature distribution using Eq. (11).

Willmore energy

The Willmore energy (W, in mm^{-2}) is defined as:

$$W = \frac{1}{S}\int_S H^2\,ds - \frac{1}{S}\int_S K\,ds \tag{12}$$

Expressed in terms of the principal curvatures, this becomes:

$$W = \frac{1}{4S}\int_S (\kappa_1 - \kappa_2)^2\,ds \tag{13}$$

This quantity is an alternative formulation of the classical Willmore functional $\mathcal{W} = \int_S H^2\,\mathrm{d}S$, commonly used in differential geometry as a measure of the bending energy of closed surfaces (e.g., Pinkall and Gross, 2024). As defined here, the Willmore energy quantifies the local difference between the two principal curvatures over the ice surface. It is locally equal to zero when the two principal curvatures are equal, as on a sphere, or when both vanish, as on a plane. Consequently, it quantifies the extent to which the grain surface deviates from being spherical or planar, providing a measure of the local shape contrast. For snow microstructures, it therefore remains low for smooth rounded surfaces and extensive planar facets, while increasing with the development of surface features such as sharp edges, ridges, and striations. The Willmore energy was derived from the mean and Gaussian curvature distributions using Eq. (12).

Specific genus

The Euler characteristic χ describes the topology of the microstructure (Richeson, 2010). It is a topological invariant: a torus and a cup with a handle have the same Euler characteristic. For a closed surface, the Euler characteristic of the surface $\chi(S)$ is related to the integral of the Gaussian curvature by the Gauss-Bonnet theorem:

$$\chi(S) = \frac{1}{2\pi}\oint_S K\,ds \tag{14}$$

https://doi.org/10.5194/egusphere-2026-4897
Preprint. Discussion started: 31 August 2026

The genus (g, dimensionless) can be interpreted as the number of handles, or independent loops, in the porous medium, and provides information about the connectivity of the grains. The genus is related to the Euler characteristic through:

$$g = N - \frac{\chi(S)}{2} \tag{15}$$

with N the number of boundaries, or the number of ice objects and air bubbles. For a single closed surface without bubbles, Eq. (15) yields $g = 1 - \frac{\chi(S)}{2}$, as used for snow in Schleef et al. (2014b). Because the genus is physically more intuitive than the Euler characteristic, and because the number of boundaries carries little information here, we present the temporal evolution of the genus instead of the Euler characteristic. Because both the Euler characteristic and the genus depend on the amount of material considered, we normalized the genus by the snow mass. The resulting specific genus (in kg^{-1}) enables comparisons between samples of different densities.

In the present work, we computed the Euler characteristic of the surface and the number of boundaries using the open-source library DGtal (DGtal) after closing the borders of the images. The Euler characteristic of the surface was computed as the number of vertices minus the number of edges plus the number of faces. The genus was derived from the Euler characteristic of the surface using Eq. (15).

3 Description of the temporal evolution of grain size and shape

This section describes the temporal evolution of the grain-size and grain-shape descriptors during dry snow metamorphism. Scalar descriptors are presented first, followed by the chord length and mean curvature distributions. While scalar descriptors provide average characteristics, distributions capture the full range of sizes and shapes, revealing additional information on their heterogeneity.

3.1 Scalar descriptors of grain size and shape

DF samples

Figure 1 shows the evolution of the size and shape descriptors for the DF samples (decomposing and fragmented particles) under ETM (-3 and -8°C) and TGM (10, 40, and 100 K m^{-1} at -3°C).

Initially, the DF samples exhibit an optical diameter of about 0.12 mm, corresponding to a high SSA of approximately 58 $\mathrm{m}^2\ \mathrm{kg}^{-1}$, characteristic of freshly deposited snow. During metamorphism, the optical diameter increases under all conditions, reaching about 0.17 mm under ETM and 0.32 mm under a temperature gradient of 100 K m^{-1}. This increase reflects the systematic decrease in SSA, which is particularly rapid during the initial stage, as commonly reported for high-SSA snow (Legagneux and Dominé, 2005). The SSA decay rate strongly depends on the temperature gradient: at -3°C, it is $-2.8\ \mathrm{m}^2\ \mathrm{kg}^{-1}\ \mathrm{day}^{-1}$ under ETM and nearly doubles to $-5.3\ \mathrm{m}^2\ \mathrm{kg}^{-1}\ \mathrm{day}^{-1}$ under 100 K m^{-1}.

https://doi.org/10.5194/egusphere-2026-4897
Preprint. Discussion started: 31 August 2026

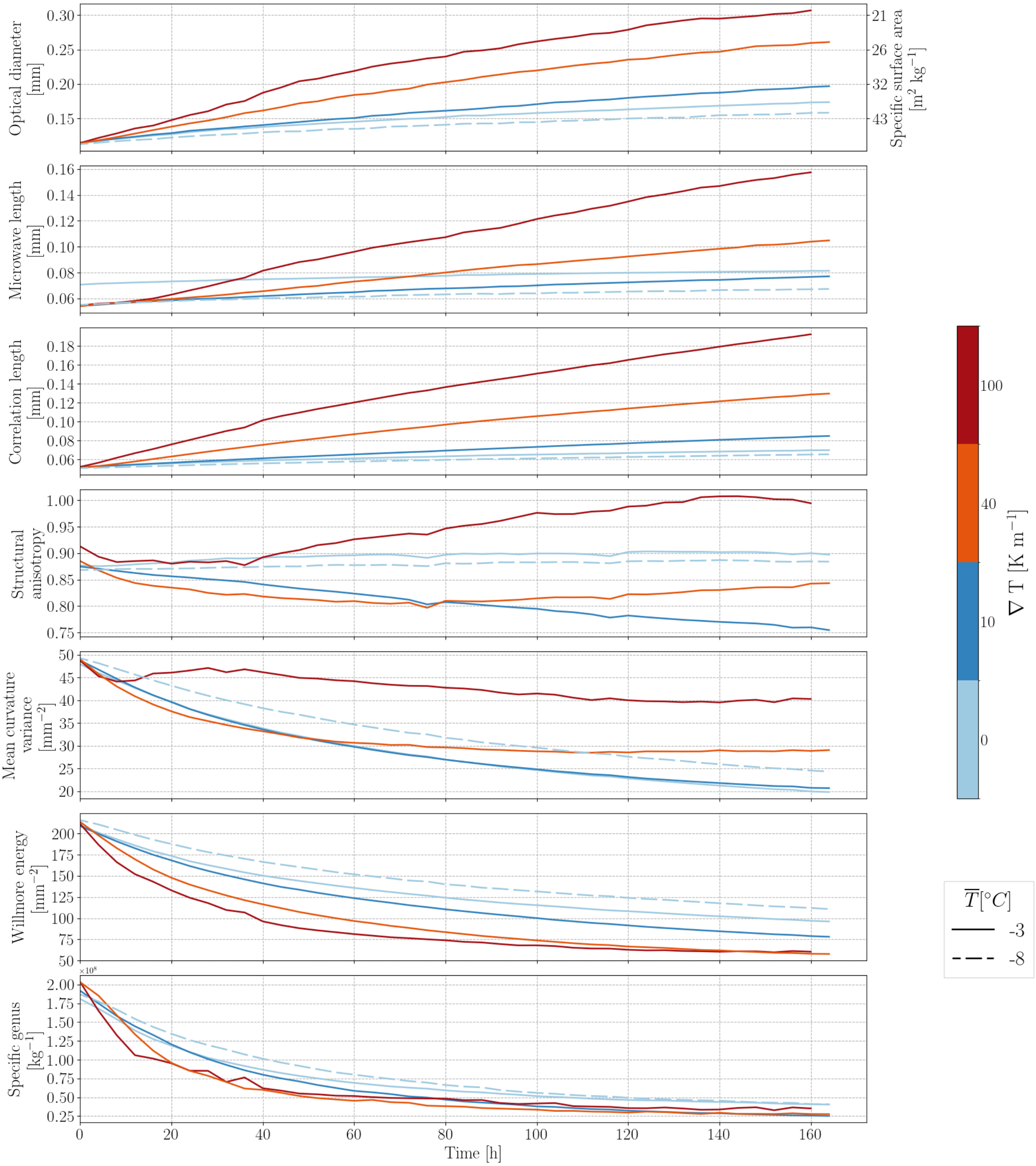

Figure 1. Temporal evolution of grain-size and grain-shape descriptors for the DF samples.

https://doi.org/10.5194/egusphere-2026-4897
Preprint. Discussion started: 31 August 2026

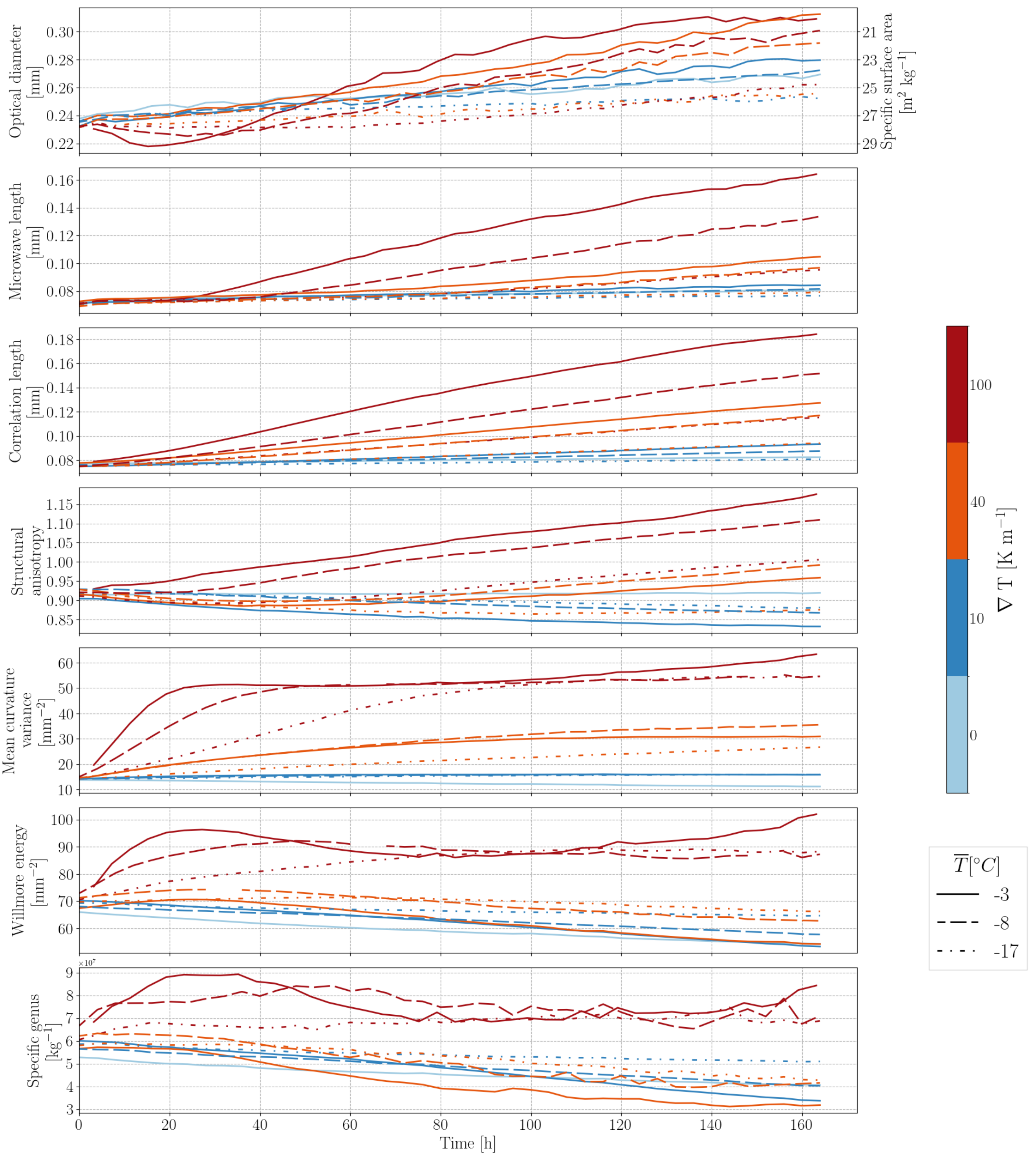

Figure 2. Temporal evolution of grain-size and grain-shape descriptors for the RGl samples.

https://doi.org/10.5194/egusphere-2026-4897
Preprint. Discussion started: 31 August 2026

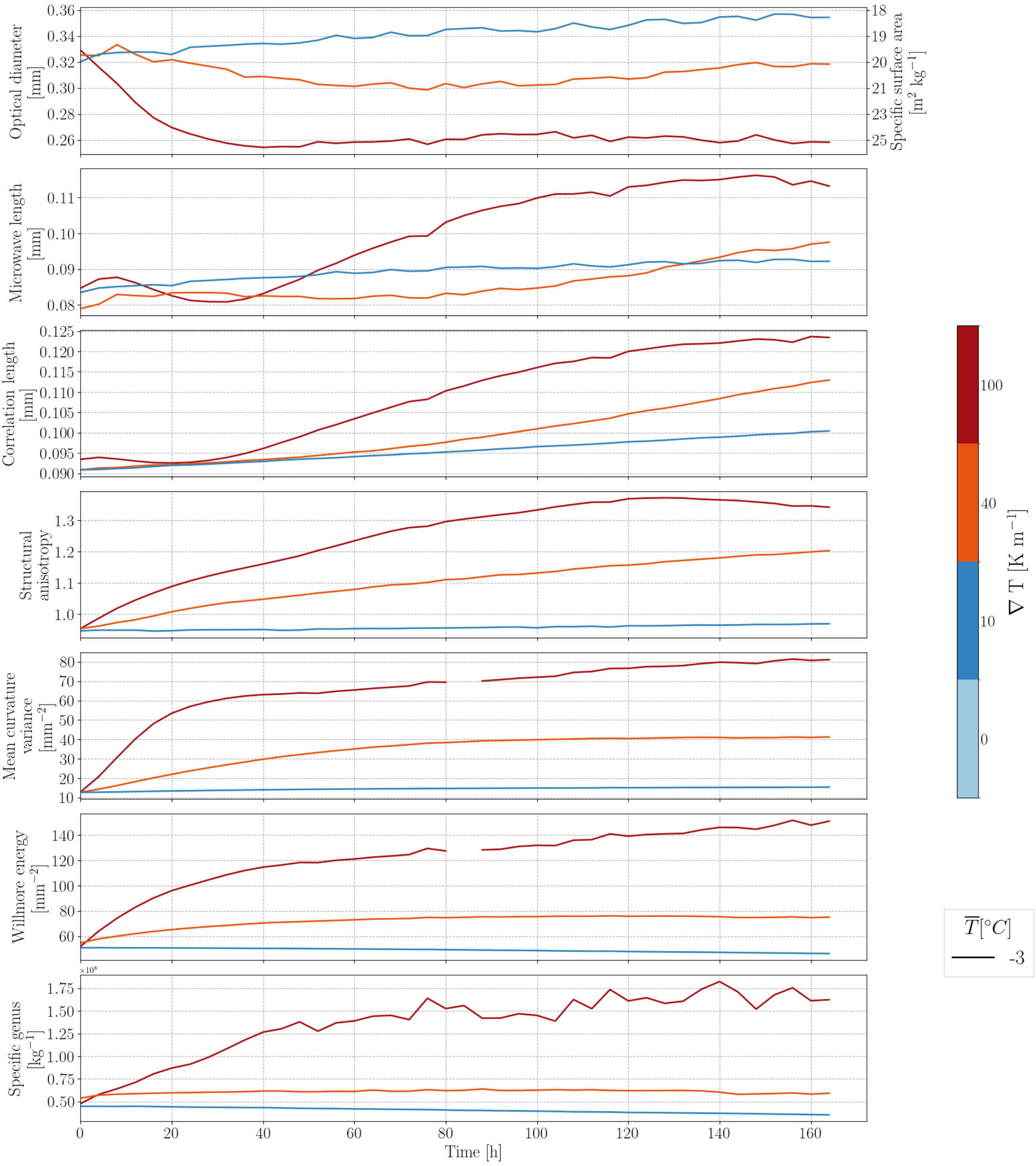

Figure 3. Temporal evolution of grain-size and grain-shape descriptors for the RGd samples.

https://doi.org/10.5194/egusphere-2026-4897
Preprint. Discussion started: 31 August 2026

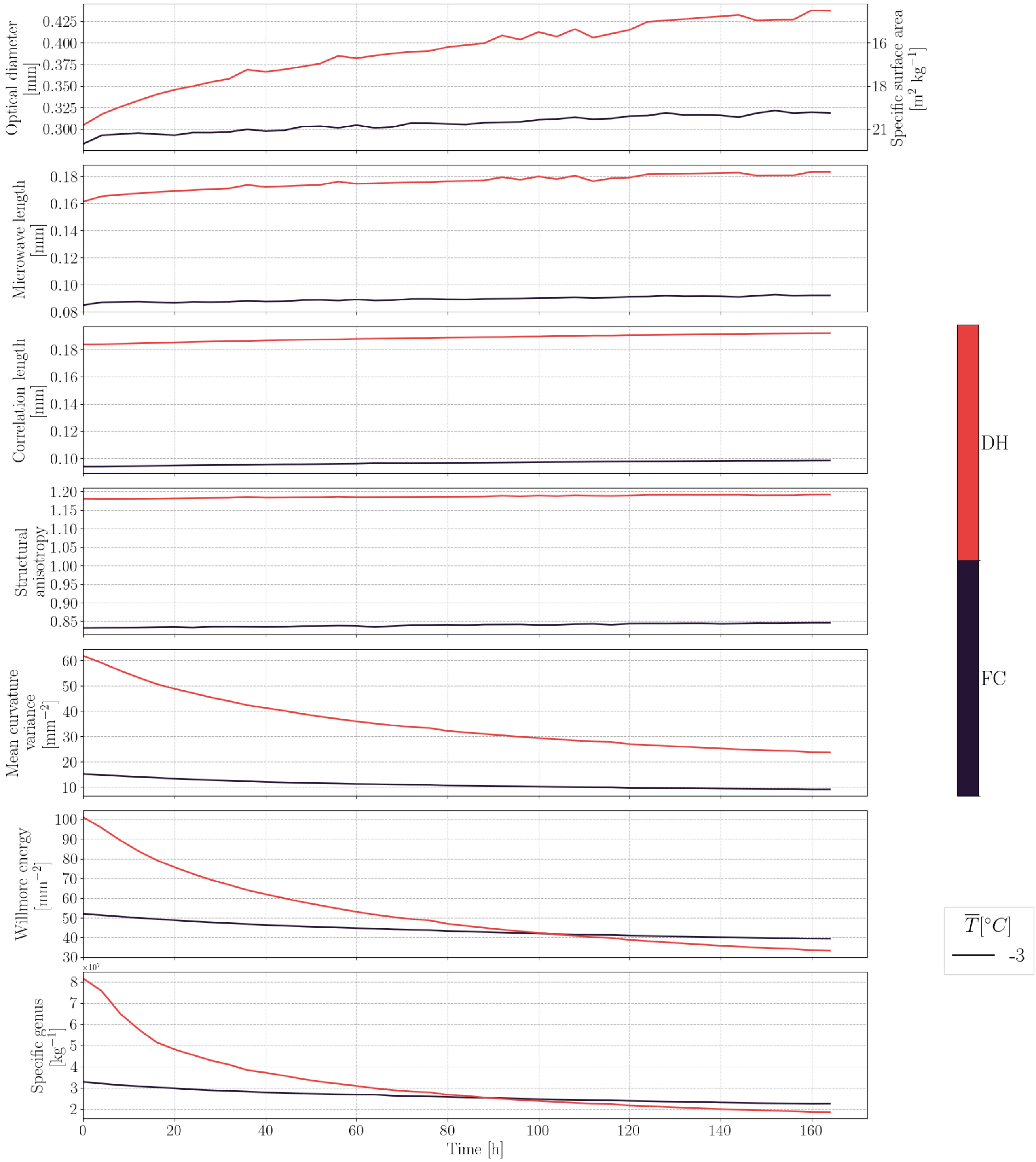

Figure 4. Temporal evolution of grain-size and grain-shape descriptors for the FC and DH samples.

https://doi.org/10.5194/egusphere-2026-4897
Preprint. Discussion started: 31 August 2026

The microwave grain size and correlation length start from substantially lower values of about 0.055 mm and increase gradually with time. Increasing the temperature gradient accelerates the evolution of both descriptors: after 7 days, their values are more than twice as large under 100 K m^{-1} as under 10 K m^{-1}. Reducing the temperature under ETM mainly slows their evolution.

In contrast to the previous descriptors, the anisotropy ratio does not exhibit a monotonic response to the temperature gradient. Initially, DF samples show a slight horizontal anisotropy, with values between 0.87 and 0.91, reflecting a preferential horizontal orientation of the ice structure. Under 100 K m^{-1}, the anisotropy gradually increases towards 1, indicating the loss of the initial anisotropy. At 40 K m^{-1}, it first decreases from 0.87 to 0.80 before returning close to its initial value, whereas at 10 K m^{-1}, it continuously decreases to 0.75, indicating a reinforcement of the initial horizontal arrangement. Under ETM, no significant changes are observed.

Finally, the DF samples are characterized by very high initial values of mean curvature variance, Willmore energy, and specific genus, compared to the values obtained for the other samples (see sections hereinbelow). It reflects their heterogeneous surface curvatures and complex, non-spherical grain shapes. All three descriptors decrease during metamorphism, although their response depends on the metamorphism regime. The mean curvature variance decreases faster under ETM and weak TGM than under 100 K m^{-1}, indicating that rounded grains and faceted crystals develop more uniform surface curvatures than highly-developed depth hoar. Conversely, the Willmore energy and the specific genus show a smaller sensitivity to the temperature gradient. Reducing the temperature from -3°C to -8°C slows down the evolution of all three descriptors under ETM without modifying their general trends.

RGl samples

Figure 2 shows the evolution of the size and shape descriptors during ten experiments conducted on RGl samples (light rounded grains): one ETM experiment at -3°C and nine TGM experiments combining gradients of 10, 40 and 100 K m^{-1} with mean temperatures of -3, -8 and -17°C. For the experiment at 100 K m^{-1} and -3°C, the first scan was acquired after a delay of 3 h 20 min and the curves were shifted accordingly. Curvature-based descriptors could not be calculated at 60 and 152 h for the experiment at 100 K m^{-1} and -8°C.

The RGl samples initially exhibit an optical diameter of about 0.24 mm, corresponding to an SSA of approximately 28 m^2 kg^{-1}. Under ETM and temperature gradients of 10 and 40 K m^{-1}, the optical diameter increases gradually as SSA decreases. Higher temperature gradients accelerate this evolution, whereas lower temperatures slow it down. For example, the SSA decay rate is 0.5 m^2 kg^{-1} day^{-1} under ETM and 0.95 m^2 kg^{-1} day^{-1} under 40 K m^{-1} at -3°C, but only 0.4 m^2 kg^{-1} day^{-1} under 40 K m^{-1} at -17°C. Different combinations of temperature and temperature gradient can also produce similar evolutions; for instance, the SSA evolution under ETM at -3°C closely matches that under 10 K m^{-1} at -8°C. A distinct behavior is observed under 100 K m^{-1}, with an initial transient stage. The optical diameter first decreases before increasing, reflecting a transient increase in SSA. At -3°C, SSA increases by about 2 m^2 kg^{-1} during the first 12 h, corresponding to a temporary decrease in optical diameter of about 0.013 mm. As temperature decreases, this transient stage becomes longer, while the magnitude of the initial decrease in optical

https://doi.org/10.5194/egusphere-2026-4897
Preprint. Discussion started: 31 August 2026

diameter becomes smaller. At −17°C, no transient decrease is observed and the optical diameter remains nearly constant for about 60 h before slightly increasing.

The microwave grain size and correlation length exhibit simpler evolutions. Both start from similar initial values (about 0.07 mm) and increase under all conditions. Increasing the temperature gradient accelerates the evolution of both descriptors, whereas decreasing the temperature slows it down. Under 100 K m^{-1} at -3°C, both descriptors more than double over 7 days, with a growth rate of 0.013 mm day^{-1}, compared with only 0.002 mm day^{-1} under 10 K m^{-1}. Under 100 K m^{-1} at -3°C and -8°C, the microwave grain size remains nearly constant during the first 20 and 30 h, respectively, before increasing. At 100 K m^{-1}, lowering the temperature from -3°C to -17°C reduces the microwave grain-size growth rate from 0.013 to 0.003 mm day^{-1}. Different combinations of temperature and temperature gradient can produce comparable evolutions, such as 40 K m^{-1} at -17°C and 10 K m^{-1} at -8°C.

As observed for the DF samples, the anisotropy ratio exhibits contrasting responses depending on the applied temperature gradient. Initially, the RGl samples show a slight horizontal anisotropy (0.90–0.93). As for DF, ETM does not significantly modify this initial state, whereas a weak temperature gradient (10 K m^{-1}) progressively reinforces the initial horizontal orientation, with the anisotropy reaching 0.83 at -3°C. Increasing the temperature gradient progressively weakens the horizontal anisotropy and, at 100 K m^{-1}, develops a vertical one. At -3°C, the anisotropy reaches 0.96 under 40 K m^{-1} and 1.18 under 100 K m^{-1} after 7 days. Again, lower temperatures mainly slow these evolutions, with the strongest effects observed at -17°C.

The curvature-based descriptors reveal marked differences between ETM, weak TGM, and strong TGM, in contrast to the systematic decreases observed for the DF samples. The initial mean curvature variance is much lower than for the DF samples, reflecting the more homogeneous surface curvatures of rounded grains. Under ETM, the surface curvatures become even more uniform, with their variance decreasing by about 20 % at -3°C. Conversely, surface curvatures become more heterogeneous under temperature gradients, with the increase becoming larger as the gradient strengthens. After 7 days, at -3°C, the mean curvature variance increases by about 10 % under 10 K m^{-1}, doubles under 40 K m^{-1} and triples under 100 K m^{-1}. Under 100 K m^{-1}, most of the increase occurs at the beginning, during the first 20–30 h at -3°C, after which the curves approach a plateau. This indicates that the largest changes in surface curvature heterogeneity occur during the early stages of strong TGM. Lower temperatures mainly extend this initial growth period without substantially affecting the final values reached after 7 days.

The Willmore energy exhibits a different response to the metamorphism conditions than the mean curvature variance. Under ETM, it decreases monotonically (about 20% at -3°C), which is consistent with the formation of rounder grains. A similar decrease is observed under a temperature gradient of 10 K m^{-1}, despite the formation of facets. More unexpectedly, a slight net decrease is also observed under 40 K m^{-1}, whereas a non-monotonic increase is observed under 100 K m^{-1}. Hence, the Willmore energy responds differently during the formation of depth hoar depending on the gradient intensity, likely related to the degree of striation and angularity of the formed depth hoar.

https://doi.org/10.5194/egusphere-2026-4897
Preprint. Discussion started: 31 August 2026

Finally, the specific genus exhibits a broadly similar dependence on temperature gradient to the Willmore energy. It indicates a slight decrease in the number of handles under ETM and 10 K m^{-1}, while 100 K m^{-1} produces a net increase after 7 days, reflecting strong topological variations.

RGd samples

Figure 3 shows the temporal evolution of the descriptors during TGM experiments on the RGd samples (dense rounded grains) subjected to temperature gradients of 10, 40, and 100 K m^{-1} at a mean temperature of -3°C. Curvature at 80 hours could not be computed for 100 K m^{-1}. As for the DF and RGl samples, the temperature gradient strongly controls the evolution of all descriptors. However, the response of the RGd samples differs markedly from the other snow types, particularly for SSA and the optical diameter.

The RGd samples initially exhibit an optical diameter of about 0.33 mm, corresponding to an SSA of around 20 m^2 kg^{-1}. The optical diameter exhibits a strong dependence on temperature gradient. Under 100 K m^{-1}, the optical diameter decreases markedly from 0.33 to 0.25 mm, associated with a rapid SSA increase of about 6 m^2 kg^{-1} during the first 40 h. At 40 K m^{-1}, both descriptors remain nearly constant, whereas at 10 K m^{-1} the optical diameter increases slightly from 0.33 to 0.35 mm, corresponding to an SSA decrease to about 18 m^2 kg^{-1}.

The microwave grain size and the correlation length differ markedly from the optical diameter, both in their absolute values and temporal evolution. Their initial values, ranging from 0.080 to 0.095 mm, are about a third of the optical diameter. Both descriptors increase under all temperature gradients, indicating overall grain coarsening, in contrast to the optical diameter. However, this increase is not steady, with little evolution during the first ∼40 h, corresponding to the period of rapid SSA increase. The coarsening rates increase with temperature gradient, reaching on average 0.0035–0.004 mm day^{-1} at 100 K m^{-1} compared to about 0.001 mm day^{-1} at 10 K m^{-1} for both descriptors.

The RGd samples exhibit the weakest initial anisotropy of the three snow types (anisotropy ratio ≈ 0.95). Unlike the DF and RGl samples, no reinforcement of the initial horizontal anisotropy is observed. Instead, all temperature gradients promote the development of a vertical anisotropy, which remains limited at 10 K m^{-1} (0.97) but becomes pronounced at 40 and 100 K m^{-1}, reaching 1.2 and 1.34, respectively.

The curvature-based descriptors also show a strong dependence on the temperature gradient. The mean curvature variance and the Willmore energy both exhibit limited changes at 10 K m^{-1}, but increase markedly at 40 and 100 K m^{-1}. This increase reflects a more dispersed distribution of the mean curvatures and principal curvatures along the surface, i.e., an increase in the surface heterogeneities or complexity of the grain surface geometry. Finally, the specific genus decreases slightly at 10 K m^{-1}, remains nearly constant at 40 K m^{-1}, and increases strongly at 100 K m^{-1}.

https://doi.org/10.5194/egusphere-2026-4897
Preprint. Discussion started: 31 August 2026

FC and DH samples

Figure 4 shows the evolution of the descriptors during equi-temperature metamorphism at -3°C for one FC sample and one DH sample.

The FC and DH samples initially exhibit optical diameters of about 0.28 and 0.30 mm, corresponding to SSA values of about 23 and 21.5 m^2 kg^{-1}, respectively. The optical diameter increases for both samples throughout ETM as SSA decreases. The evolution is much larger for the DH sample, with the optical diameter rising from 0.30 to 0.44 mm (rate of 0.02 mm day^{-1}), corresponding to an SSA decrease to 15 m^2 kg^{-1} (rate of -0.92 m^2 kg^{-1} day^{-1}). In contrast, the FC sample exhibits only a slight increase in optical diameter, corresponding to a decrease in SSA to 20.5 m^2 kg^{-1} (rate of -0.37 m^2 kg^{-1} day^{-1}). The stronger SSA decrease for the DH sample is consistent with the progressive smoothing of its striated and angular surfaces.

The initial microwave grain size and correlation length are similar, with values of about 0.085–0.095 mm for the FC sample and 0.16–0.18 mm for the DH sample. Both descriptors increase only slightly during ETM (rates of 0.0003 mm day^{-1} for DH and 0.001 mm day^{-1} for FC), indicating limited coarsening for both snow types.

The FC and DH samples inherit the anisotropy acquired during the TGM experiment: initially, the FC sample exhibits a horizontal anisotropy (0.83), whereas the DH sample exhibits a vertical anisotropy (1.18). ETM produces almost no change in either sample, indicating that this process preserves the initial structural orientation.

Finally, the FC and DH samples also differ markedly in their initial curvature-based descriptors. The mean curvature variance, Willmore energy, and specific genus are substantially higher for the DH sample, reflecting more heterogeneous surface curvatures and a higher connectivity than the FC sample. During ETM, all three descriptors decrease, with much larger reductions for the DH sample than for the FC sample. These trends indicate a progressive smoothing of the grain surfaces together with a decrease in the connectivity of the ice network. Consequently, the differences between the FC and DH samples diminish during ETM, particularly for the Willmore energy and the specific genus.

3.2 Chord length distributions

Next, we investigate the evolution of the chord length distributions to characterize the full range of length scales within the snow microstructure. This analysis provides further insight into the evolution of the scalar grain-size descriptors presented above, in particular the optical diameter (or SSA) and the microwave grain size, which are both closely related to the chord length distribution.

3.2.1 Evolution during the TGM experiments

The evolution of the chord length distributions during temperature-gradient metamorphism is presented in Figure 5. Changes occur in both the mean and the spread of the distributions and depend on the initial snow type and the applied temperature gradient. The minimum chord length displayed corresponds to the size of 2 voxels (16.90 μm).

https://doi.org/10.5194/egusphere-2026-4897
Preprint. Discussion started: 31 August 2026

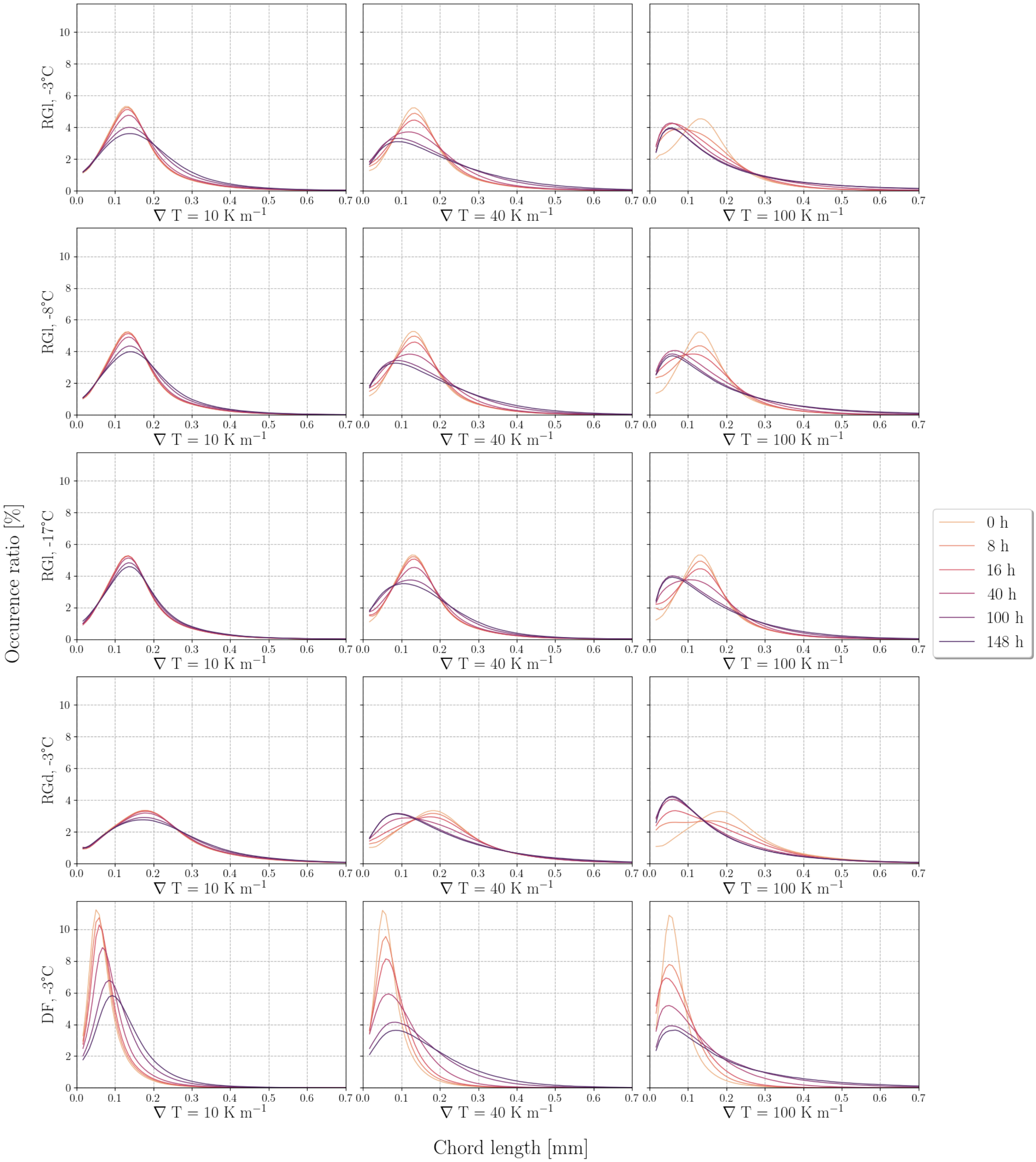

Figure 5. Histograms of chord lengths at six time steps during temperature-gradient metamorphism for the RGl, RGd and DF samples. For the experiment at 100 K m^{-1} and -3°C, the first scan (0 h) was acquired 3 h 20 min after the start of the experiment.

https://doi.org/10.5194/egusphere-2026-4897
Preprint. Discussion started: 31 August 2026

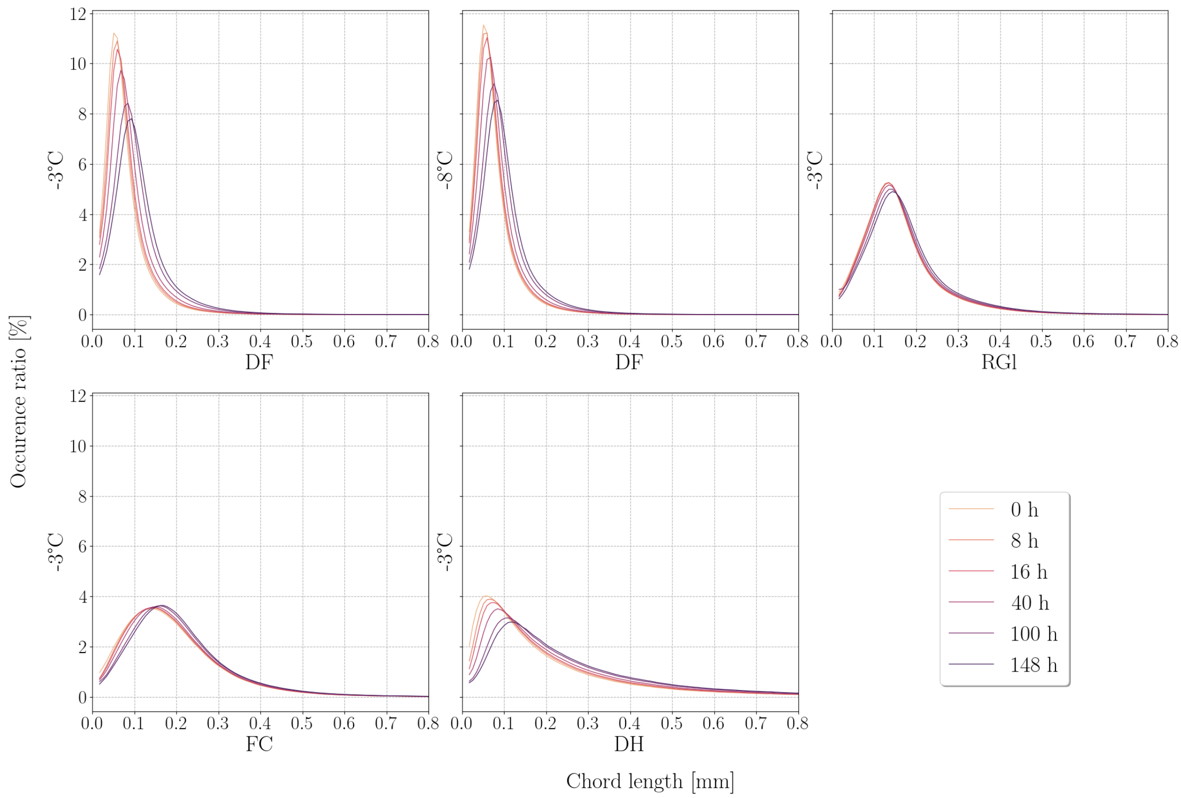

Figure 6. Histograms of chord lengths at six time steps during equi-temperature metamorphism for the DF, RGl, FC and DH samples.

The RGl samples initially exhibit a unimodal distribution centered near 0.13 mm, with maximum chord lengths of approximately 0.5–0.6 mm. A temperature gradient of 10 K m^{-1} mainly widens the distribution towards larger chord lengths, indicating overall grain coarsening. Gradients of 40 and 100 K m^{-1} broaden the distribution by simultaneously increasing the proportion of short chords (below 0.1 mm) and long chords (between 0.25 and 0.5 mm). Hence, unlike the scalar size descriptors, the chord length distributions reveal that the formation of larger grains occurs alongside the development of finer ice features under TGM. For all gradients, decreasing the mean temperature primarily slows down the evolution.

Compared with the RGl samples, the RGd samples exhibit a broader initial distribution centered around 0.19 mm, with the longest chords reaching 0.7 mm, but undergo similar changes under TGM. Long chords (0.3–0.5 mm) become slightly more frequent at 10 K m^{-1}, whereas short chords (below 0.15 mm) become increasingly frequent at 40 and 100 K m^{-1}, reflecting the formation of finer ice structures such as striations.

The DF samples exhibit a distinct initial distribution, with a peak centered around 0.07 mm and maximum chord lengths of only about 0.3 mm. Under all temperature gradients, the distributions move towards larger chord

https://doi.org/10.5194/egusphere-2026-4897
Preprint. Discussion started: 31 August 2026

lengths, indicating grain coarsening, while simultaneously broadening, indicating increasing size heterogeneity. This broadening becomes more pronounced as the temperature gradient increases: after 7 days, the maximum chord length reaches about 0.7 mm under 100 K m^{-1}, compared with about 0.4 mm under 10 K m^{-1}.

3.2.2 Evolution during the ETM experiments

Figure 6 shows the evolution of the chord length distributions during equi-temperature metamorphism. In contrast to TGM, ETM produces similar changes across snow types. The distributions evolve towards larger chord lengths, consistent with microstructural coarsening. The magnitude of the evolution, however, varies between snow types: it is smallest for the RGl and FC samples and largest for the DF and DH samples, which show the greatest increase in long chord lengths. A concurrent reduction in short chords is also observed, which likely results from the smoothing of grain striations in the DH samples, whereas it reflects overall grain coarsening in the DF samples. Consistent with the scalar size descriptors, lowering the temperature mainly slows the evolution without modifying the overall distribution shape.

3.3 Mean curvature distributions

Next, we investigate the evolution of the mean curvature distributions to characterize the diversity of local surface curvatures within the snow microstructure and their evolution during metamorphism. These distributions complement the scalar curvature-based descriptors presented above by capturing the evolution of the entire curvature range.

3.3.1 Evolution during the TGM experiments

Figure 7 shows the evolution of mean curvature distributions during temperature-gradient metamorphism. To relate the distribution features to actual grain shapes, 3D images of the snow microstructure are provided in Fig. 8. The distributions are first analyzed for the RGl samples to identify the main changes associated with the different temperature gradients. The distributions of the RGd and DF samples are then examined to assess the influence of the initial snow microstructure on these changes.

The RGl samples initially exhibit a unimodal distribution centered around 8 mm^{-1}, indicating predominantly convex grain surfaces. The negative curvatures mainly correspond to grain necks and the highest positive curvatures to ice protuberances (Fig. 8a). Consistent with the curvature-based descriptors, distinct changes in the distributions emerge depending on the applied temperature gradient. Under 10 K m^{-1}, the distribution progressively becomes bimodal. The main peak shifts from about 8 to 5 mm^{-1}, reflecting surface coarsening, while a secondary peak develops around 0 mm^{-1} as flat facets form, as shown in Fig. 8d. Although the distribution tails change little quantitatively, their physical meaning evolves: high positive curvatures become associated mainly with facet edges rather than rounded protuberances. In contrast, gradients of 40 and 100 K m^{-1} produce markedly different distributions,

https://doi.org/10.5194/egusphere-2026-4897
Preprint. Discussion started: 31 August 2026

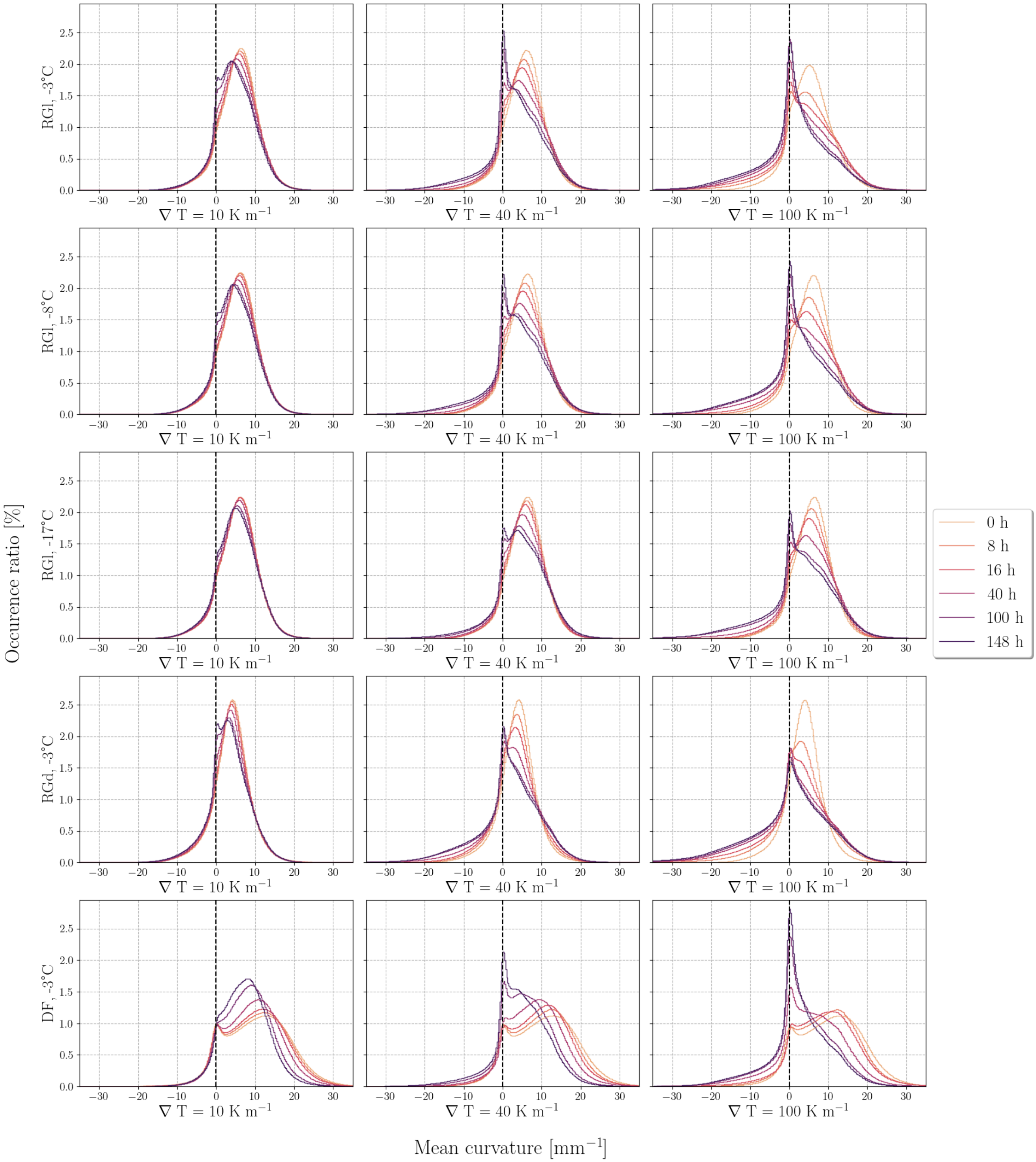

Figure 7. Histograms of mean curvature for RGl, RGd and DF samples at six time steps. For the experiment at 100 K m^{-1} and -3°C, the first scan (0 h) was acquired 3 h 20 min after the start of the experiment.

https://doi.org/10.5194/egusphere-2026-4897
Preprint. Discussion started: 31 August 2026

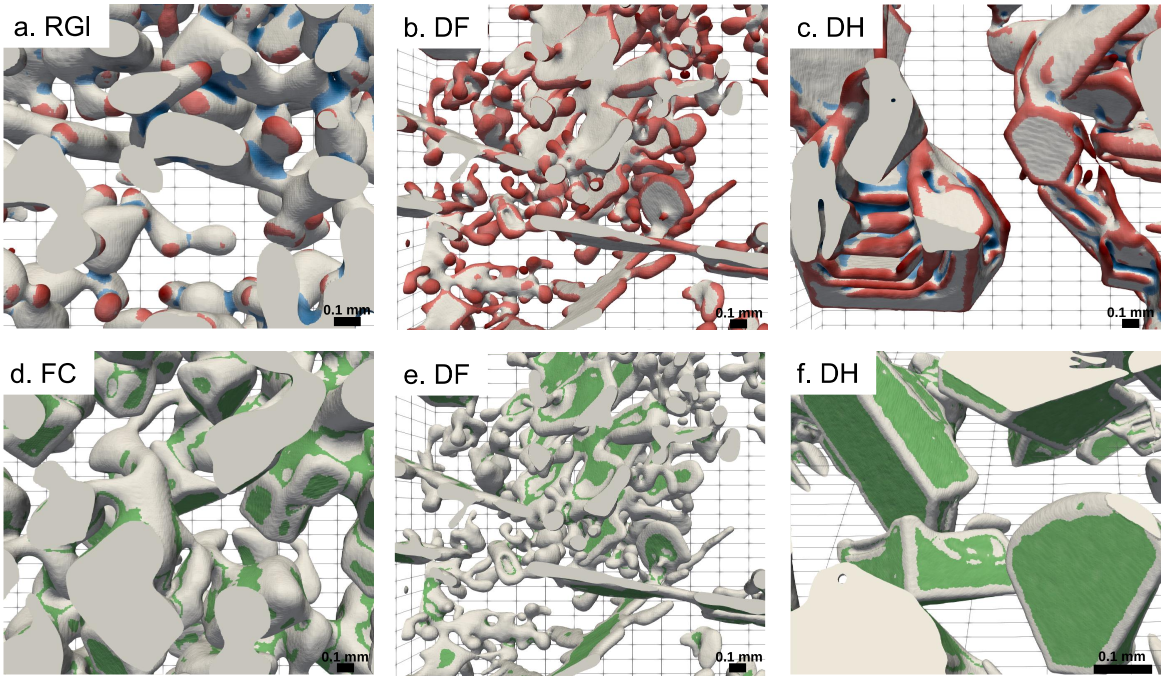

Figure 8. Relationship between snow grain features and mean curvature values. 3D renderings of selected snow microstructures with the ice-air interface colored according to specific intervals of mean curvature. A 0.85 mm-thick vertical image slice is shown. Blue shows negative mean curvatures, red shows positive mean curvatures, and green shows mean curvatures close to zero. Panels show (a) an initial RGl sample, (b,e) an initial DF sample, (c,f) a DH sample, and (d) a FC sample. The curvature intervals are: (a) blue: -20 to 0 mm^{-1}, red: 12 to 30 mm^{-1}; (b,e) red: 10 to 40 mm^{-1}, green: -2 to 2 mm^{-1}; (c,f) blue: -25 to -5 mm^{-1}, red: 5 to 25 mm^{-1}, green: -2 to 2 mm^{-1}; (d) green: -1.5 to 1.5 mm^{-1}.

characteristic of depth hoar formation. After a transient bimodal stage, the positive peak disappears, and the final distribution is dominated by a sharp peak centered near 0 mm^{-1} with long asymmetric tails. The increase in near-zero curvatures at the expense of positive curvatures reflects the development of large faceted surfaces (Fig. 8) at the expense of rounded surfaces. The distribution tails also evolve. The negative tail broadens, reflecting the development of concavities within surface striations (Fig. 8c). Meanwhile, the positive tail decreases in amplitude but remains broad, associated with the formation of sharp grain edges and striations (Fig. 8c). This broadening of both distribution tails explains the increase in the mean curvature variance reported in the previous section. Lower temperatures mainly slow these transformations; for example, the distributions obtained at -17°C after 148 h closely resemble intermediate stages observed at -3°C.

The RGd samples display the same overall evolution despite narrower initial distributions centered around 4 mm^{-1}. Weak gradients produce the bimodal distributions typical of faceted crystals, whereas strong gradients generate the sharp peak at zero and broad, asymmetric tails, associated with depth-hoar formation. Compared with the RGl

https://doi.org/10.5194/egusphere-2026-4897
Preprint. Discussion started: 31 August 2026

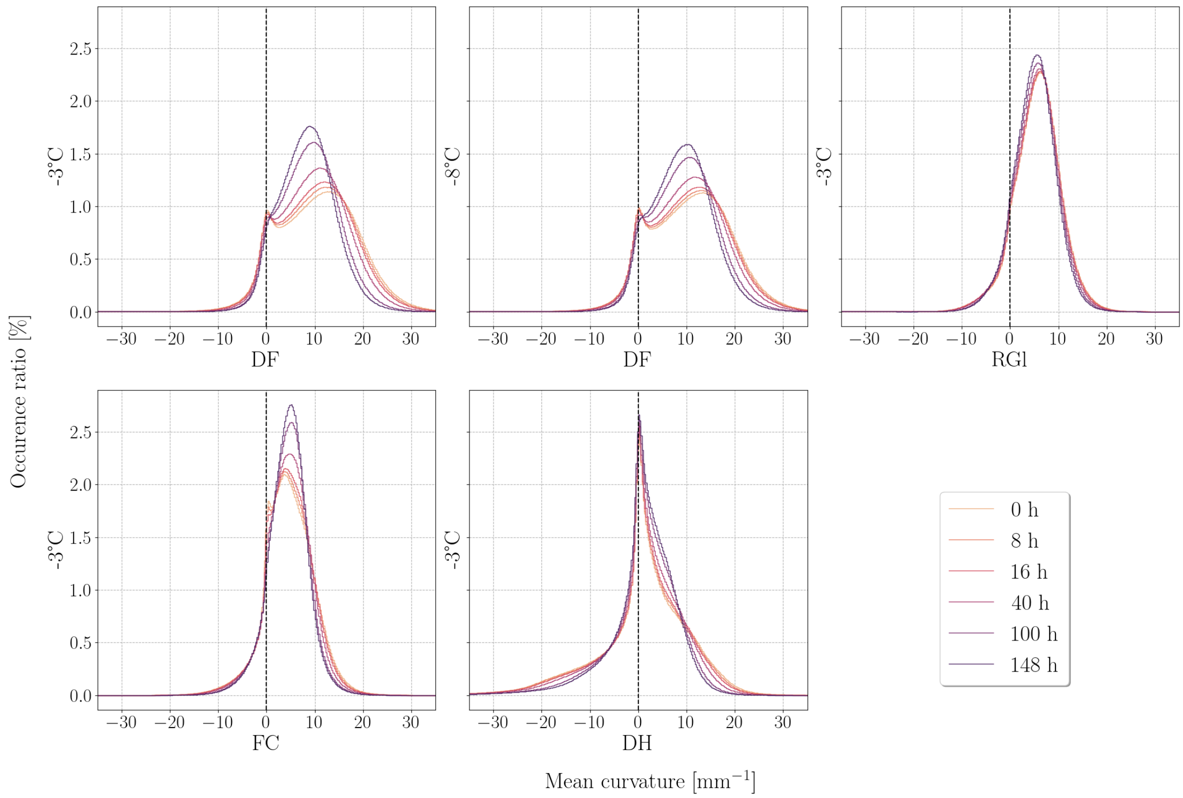

Figure 9. Histograms of mean curvature for DF, RGl, FC and DH samples at six time steps during ETM.

samples, the RGd samples develop even broader positive and negative tails, consistent with the stronger development of striated surfaces.

Unlike the RGl and RGd samples, the DF samples exhibit a broad initial distribution composed of a main peak around 13 mm^{-1} and a secondary peak near 0 mm^{-1}. The latter reflects the flat surfaces inherited from plate-like precipitation particles (Fig. 8e), whereas the broad positive peak results from the coexistence of decomposing and fragmented particles and graupel (Fig. 8b). Despite this different starting point compared to rounded grains, the evolution converges towards the same regimes. Under 10 K m^{-1}, the main peak shifts towards lower curvatures (about 9 mm^{-1}) indicating surface coarsening, while the secondary peak remains nearly unchanged, reflecting faceting. The large reduction of the positive tail of the distribution reflects the progressive disappearance of highly convex graupel features. In contrast, under 40 and 100 K m^{-1}, the main peak gradually vanishes, and the distribution evolves towards the asymmetric peak centered at zero that characterizes depth hoar.

https://doi.org/10.5194/egusphere-2026-4897
Preprint. Discussion started: 31 August 2026

3.3.2 Evolution during the ETM experiments

Figure 9 presents the evolution of the mean curvature distributions during equi-temperature metamorphism. Unlike TGM, ETM systematically smooths the curvature distributions by reducing extreme positive and negative curvatures and promoting more rounded grain surfaces. The magnitude of this evolution, however, depends on the initial snow type. For the DF samples, the initial bimodal distribution evolves towards a unimodal distribution centered near 10 mm^{-1}. The secondary peak disappears, and the positive tail shortens as the highly convex graupel features progressively vanish. Similar changes occur at -8°C but at a slower rate. The RGl samples undergo only minor modifications. The distribution becomes slightly narrower and shifts towards lower curvature values, consistent with the development of a coarser and more homogeneous rounded microstructure. The FC and DH samples show two distinct responses to ETM. For the FC sample, the bimodal distribution progressively disappears, the peak around 8 mm^{-1} becomes more pronounced, and the distribution approaches that of rounded grains, reflecting the progressive rounding of facets and grain edges. In contrast, the DH sample retains its sharp peak around 0 mm^{-1}, indicating the persistence of extensive flat facets. Only the tails become narrower, consistent with the smoothing of striations and the rounding of grain edges. Hence, unlike the FC sample, the DH sample does not recover a rounded-grain distribution under ETM.

4 Analysis and discussion

The previous section described the temporal evolution of the snow microstructure observed throughout the experiments of Dick et al. (2026b). Here, we discuss the main findings on grain-size and grain-shape evolution during dry snow metamorphism, compare them with previous studies, and examine their implications for snowpack modeling.

4.1 Insights into grain size and shape evolution

The diversity of SSA evolution

SSA exhibits a wide range of temporal evolutions, as summarized in Fig. 10a. Depending on the initial snow type and the applied temperature gradient, it may decrease monotonically, remain nearly constant, or even increase.

Under ETM, SSA systematically decreases at a rate that depends on the initial microstructure and mean temperature, consistent with numerous laboratory and field observations (e.g., Cabanes et al., 2003; Legagneux et al., 2004; Taillandier et al., 2007; Kaempfer and Schneebeli, 2007; Hachikubo et al., 2014). However, although the FC and DH samples have similar initial SSA values, they exhibit markedly different decreases under ETM at −3°C: approximately 6.6 $m^2\ kg^{-1}$ for DH and only 2.5 $m^2\ kg^{-1}$ for FC during the 164 hours of experiments (Fig. 10a). Thus, our results suggest that the SSA decay rate is not only controlled by the initial SSA value. Braun et al. (2024) proposed the mean curvature variance as a controlling factor of SSA evolution under ETM, with a more heterogeneous surface curvature distribution promoting faster SSA decay. This is consistent with our results, as the mean

https://doi.org/10.5194/egusphere-2026-4897
Preprint. Discussion started: 31 August 2026

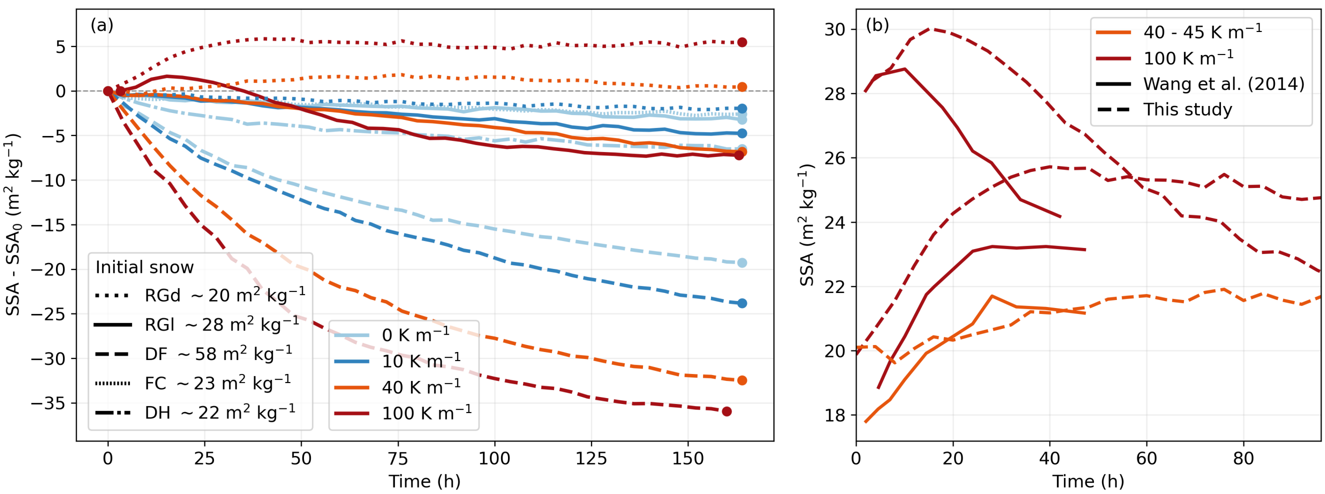

Figure 10. (a) Comparison of SSA evolution for all experiments performed at -3°C, expressed as SSA normalized by the initial value (SSA_0). The initial snow type is indicated by the line style, and its mean initial SSA is given in the legend. (b) Comparison of the SSA evolution during TGM between selected experiments from Wang and Baker (2014) and the present study using the RGl and RGd samples.

curvature variance of the DH sample is approximately four times larger than that of the FC sample. Furthermore, the DF sample, which exhibits both the highest initial SSA and the largest mean curvature variance, undergoes the largest SSA reduction (approximately 20 m^2 kg^{-1}).

In contrast to ETM, SSA exhibits a much broader range of behaviors under TGM (Fig. 10a). For the DF sample, characterized by high initial SSA and high mean curvature variance, SSA decreases systematically, consistent with previous studies on TGM (e.g., Schneebeli and Sokratov, 2004; Taillandier et al., 2007; Calonne et al., 2014a; Wang and Baker, 2014; Bouvet et al., 2023). Moreover, the SSA decrease is amplified by the temperature gradient. In contrast, snow with intermediate to low initial SSA and mean curvature variance, represented here by the RGl and RGd samples, does not exhibit a unique SSA evolution. Instead, the response depends strongly on the temperature gradient (Fig. 10a). Under a gradient of 100 K m^{-1}, SSA increases by about 5 m^2 kg^{-1} for RGd, whereas RGl shows only a transient increase during the first 12 h before decreasing, resulting in a net loss of about 7 m^2 kg^{-1}. At 40 K m^{-1}, SSA remains nearly constant for RGd but decreases gradually by about 7 m^2 kg^{-1} for RGl. At 0 and 10 K m^{-1}, SSA decreases for both snow types.

The SSA increase under strong temperature gradients for snow with intermediate to low initial SSA was first described by Domine et al. (2009) and later investigated in detail by Wang and Baker (2014) during the first 48 h of temperature-gradient metamorphism. Figure 10b compares selected experiments from the latter study with our observations. The close agreement confirms the strong influence of both the initial snow microstructure and the temperature gradient on SSA evolution. As discussed in Wang and Baker (2014), the diversity of SSA evolution

https://doi.org/10.5194/egusphere-2026-4897
Preprint. Discussion started: 31 August 2026

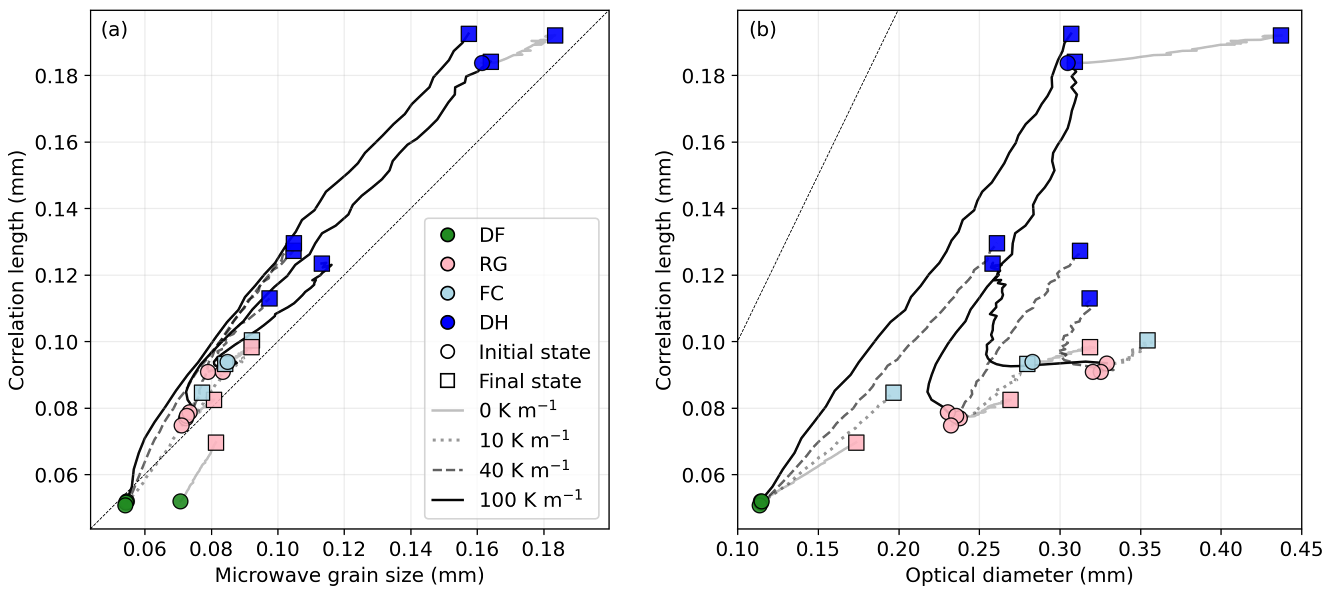

Figure 11. Comparing the grain size descriptors for all the experiments at -3°C: scatter plot of (a) the microwave grain size versus the correlation length and of (b) the optical diameter versus the correlation length. The grey lines correspond to the temporal evolution between the initial and final states.

reflects the competition between two opposing processes during TGM: grain growth, which reduces the ice surface area, and the development of surface heterogeneities due to the Mullins–Sekerka instability (Mullins and Sekerka, 1964), such as striations and hollow shapes, which increases it. Which process dominates depends on both the applied temperature gradient and the initial snow microstructure. Under 100 K m^{-1}, the rapid development of striations, skeletal interfaces and other surface irregularities can temporarily compensate for, or even exceed, the surface area loss associated with grain growth. In contrast, snow with initially high SSA already shows a highly irregular interface, leaving little potential for the formation of additional surface area. Even under high temperature gradients, grain coarsening thus dominates and SSA decreases. This confirms that the evolution of SSA cannot be interpreted solely as a measure of grain growth.

Comparing grain size descriptors

Grain size was characterized using three scalar descriptors (the optical diameter, the microwave grain size, and the correlation length) together with the chord length distributions. A comparison between the different descriptors is provided in Fig. 11.

The microwave grain size and the correlation length exhibit absolute values in the same range and consistently indicate grain coarsening during both ETM and TGM for all snow types (Fig. 11a). This is consistent with Picard et al. (2022), who showed that both descriptors are closely related and even coincide for microstructures with two-point correlation functions strictly exponential. The coarsening rates of the two descriptors increase with temperature gradient: for example, coarsening is about ten times faster at 100 than at 0 K m^{-1} for the DF samples. In contrast, the optical diameter is systematically two to three times larger than the correlation length and microwave grain size, and its evolution does not always indicate a grain size increase (Fig. 11b). During TGM, the optical diameter may either increase or decrease depending on the balance between processes that increase or decrease the snow surface area, as discussed above for SSA.

These contrasting behaviors indicate that the three descriptors probe different length scales of the snow microstructure. This is illustrated by the following two examples. During the formation of depth hoar from an RGd sample under a temperature gradient of 100 K m^{-1}, large ice structures develop simultaneously with thinner ice features such as surface striations. The development of thinner ice features is well captured by the chord length distribution, with the increase of chords shorter than 0.15 mm (Fig. 5). As a result, the optical diameter decreases (from 0.33 to 0.25 mm), whereas both the microwave grain size and the correlation length increase (from about 0.09 to 0.12 mm) (Fig. 3). A second example is the evolution of depth hoar under ETM, where surface striations and sharp edges are progressively smoothed out, while the overall dimensions of the ice structure remain nearly unchanged. Again, the smoothing of striations is well captured by the chord length distribution, with the decrease of chords shorter than 0.15 mm (Fig. 6). Accordingly, the optical diameter increases markedly (from 0.30 to 0.44 mm), whereas the microwave grain size and the correlation length show little change (Fig. 4). These examples indicate that the microwave grain size and the correlation length primarily reflect the large-scale dimensions of the ice structure, whereas the optical diameter is also sensitive to small-scale surface features. These differences are consistent with previous studies showing that optical and microwave grain metrics characterize different aspects of snow microstructure (Mätzler, 2002; Krol and Löwe, 2016). The information summarized by these scalar descriptors is captured by the chord length distributions, which simultaneously describe the evolution of both the large-scale and small-scale structural features of the ice network.

Structural anisotropy evolution

Structural anisotropy exhibits a more complex evolution than generally reported. During TGM, snow is commonly described as evolving toward a more vertically oriented ice structure because of preferential vertical heat and mass transport (Schneebeli and Sokratov, 2004; Löwe et al., 2013; Calonne et al., 2014a; Bouvet et al., 2023). As summarized in Fig. 12, we systematically observed this behavior for all samples only under the strongest temperature gradient (100 K m^{-1}). Under moderate and weak temperature gradients, the development of vertical anisotropy is not systematic. Instead, some samples evolve toward a more horizontally oriented structure. This is the case for the DF sample at 40 K m^{-1} and for both the DF and RGl samples at 10 K m^{-1}. To our knowledge, this behavior has only been reported by Wiese and Schneebeli (2017), although a direct comparison is difficult because their definition of anisotropy differs from ours. Leinss et al. (2016) suggested that the development of horizontally oriented structures may result from snow densification. However, this mechanism is unlikely to explain our observations, as little to no

https://doi.org/10.5194/egusphere-2026-4897
Preprint. Discussion started: 31 August 2026

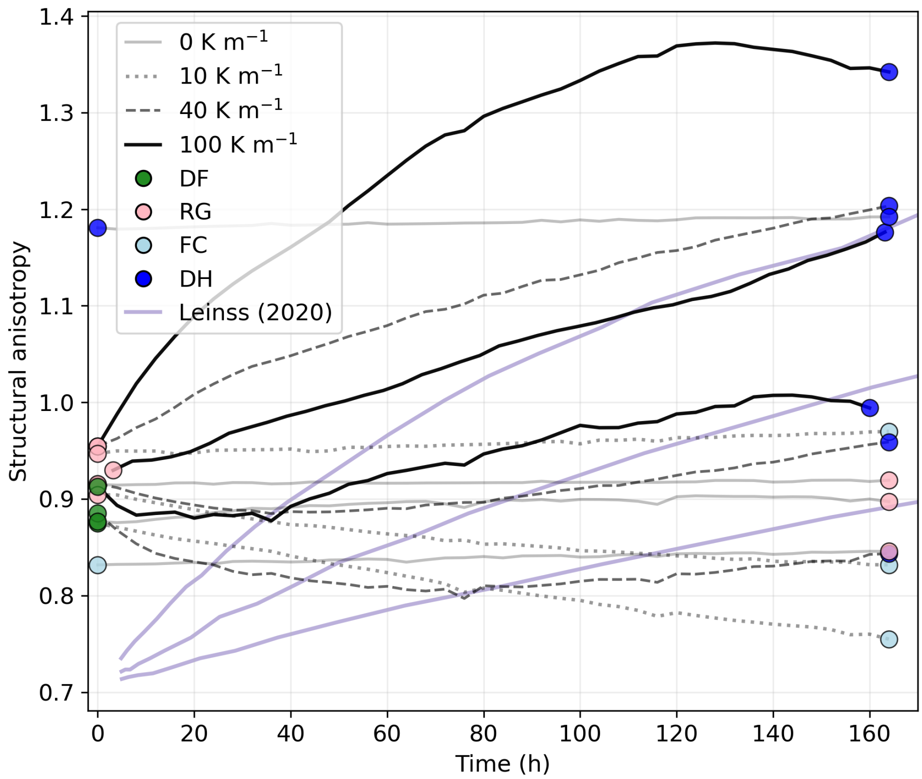

Figure 12. Overview of the structural anisotropy evolution observed in the present study. A comparison with the anisotropy modeled by Leinss et al. (2020) for temperature gradients of 25, 50, and 100 K m^{-1} at a mean temperature of 0°C is also provided (data digitized from Fig. 2a of Leinss et al. (2020)).

compaction occurred during any of the experiments (Fig. A2). Hence, the observed anisotropy evolution is primarily driven by the microstructural transformations associated with vapor transport during dry snow metamorphism.

Another important result is the strong influence of the initial snow microstructure on the evolution of structural anisotropy during TGM. For example, under identical conditions of 100 K m^{-1} at -3°C, anisotropy increases by only about 0.1 for the DF sample, compared with about 0.25 for the RGl sample and 0.4 for the RGd sample. Moreover, not only the rate but also the evolution pathway depends on the initial microstructure. This is illustrated by the two RG samples at 40 K m^{-1}: despite sharing the same snow type and similar initial anisotropies (0.95 and 0.92), the RGd sample develops a more vertically oriented structure, whereas the RGl sample first develops a slightly more horizontally oriented structure (0.88) before reversing after about 50 h, leading overall to almost no change in anisotropy after 7 days (0.96). This suggests that even small differences in the initial anisotropy, and more generally other characteristics of the initial snow microstructure, such as density, may strongly influence the development of structural anisotropy during TGM.

https://doi.org/10.5194/egusphere-2026-4897
Preprint. Discussion started: 31 August 2026

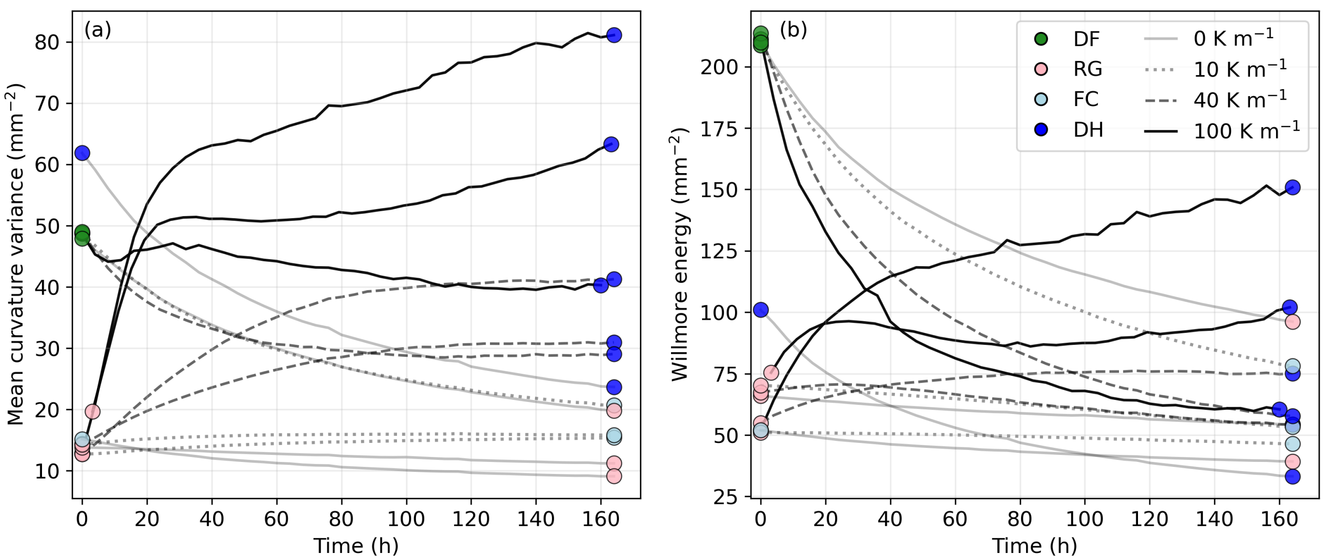

Figure 13. Summary of the evolution of the curvature-based shape descriptors during all the experiments at −3°C.

Under ETM, in contrast, the initial structural anisotropy is largely preserved (Fig. 12). Both the horizontally anisotropic FC sample and the vertically anisotropic DH sample retain their initial structural orientation throughout the experiments, consistent with the modeling results of Bouvet et al. (2022).

Finally, in addition to the anisotropy ratio based on the correlation lengths used throughout this study, an anisotropy ratio based on the mean chord lengths measured along the three Cartesian directions was also computed for comparison. The anisotropy trends are consistent between the two definitions, but their amplitudes are substantially smaller when based on the mean chord lengths (Appendix, Fig. A5). For example, for the RGd sample under 100 K m^{-1}, the anisotropy ratio increases from 0.95 to 1.34 (increase of 0.42) when computed from the correlation lengths, compared with only 0.96 to 1.10 (increase of 0.14) when computed from the mean chord lengths. This indicates that the anisotropy ratio based on the correlation length provides a more sensitive descriptor of changes in the preferential orientation of the overall ice structure.

Curvature-based grain-shape descriptors

Among the three curvature-based descriptors investigated, two characterize snow grain shape: the mean curvature variance and the Willmore energy. The mean curvature variance quantifies the heterogeneity of mean curvature across the grain surface, while the Willmore energy quantifies the deviation of the grain surface from being spherical or planar. The Willmore energy increases with the development of sharp edges and striations while remaining relatively low for both smooth rounded surfaces and extensive planar facets. Figure 13 summarizes their evolution for all experiments performed at −3°C.

https://doi.org/10.5194/egusphere-2026-4897
Preprint. Discussion started: 31 August 2026

The mean curvature variance evolves differently depending on both the initial snow microstructure and the metamorphism regime (Fig. 13a). In general, stronger temperature gradients produce larger curvature heterogeneities, increasing progressively from faceted crystals to depth hoar formed under 40 K m^{-1}, and reaching their highest values for depth hoar formed under 100 K m^{-1}. Conversely, ETM decreases the mean curvature variance through progressive surface smoothing. Across the snow types, a clear distinction can be made between FC and DH, and even between depth hoar formed under different temperature gradients. DF and DH exhibit, however, comparable mean curvature variances: in DF, the curvature heterogeneities arise primarily from highly convex dendritic branches (Fig. 8b,e), whereas in DH they arise from large angular grains with abundant surface striations (Fig. 8c,f). Likewise, the FC and RG samples cannot be clearly distinguished, as both exhibit relatively low mean curvature variance.

In contrast, the Willmore energy does not evolve systematically with the metamorphism regime (Fig. 13b). During ETM, it consistently decreases for all snow types, reflecting progressive surface smoothing. During TGM, however, its evolution depends strongly on the initial snow microstructure and no clear trend with the applied temperature gradient emerges. Across the different snow types, only DF exhibits a distinct signature, with the highest Willmore energies. RG, FC and DH show overlapping values, indicating that different snow microstructures can exhibit similar Willmore energies. In particular, rounded grains and faceted crystals can have comparable Willmore energies because, in FC, the decrease associated with the formation of large planar facets is compensated by the increase associated with the development of sharp edges, leading to an overall value similar to that of the rounded grains. The Willmore energy therefore provides limited discrimination between snow types.

4.2 Implications for snowpack modeling

Current detailed snowpack models represent the snow microstructure using only a limited set of microstructural descriptors (Vionnet et al., 2012; Lehning et al., 2002; Lafaysse et al., 2025). They predict a single grain-size descriptor, the optical diameter through the evolution of SSA, together with empirical grain-shape descriptors such as the sphericity index (Vionnet et al., 2012; Lafaysse et al., 2025) or the grain-bond connectivity index (Lehning et al., 2002).

Different snow applications, however, require additional microstructural information. For example, microwave applications require a grain-size descriptor such as the microwave grain size or the correlation length (Wiesmann and Mätzler, 1999; Mätzler, 2002; Picard et al., 2022), together with structural anisotropy (Leinss et al., 2016), whereas snow optics requires grain-shape information beyond SSA (Libois et al., 2013; Krol and Löwe, 2016). Future snowpack models could therefore benefit from representing multiple complementary grain-size and grain-shape descriptors. In particular, the microwave grain size or the correlation length could be implemented alongside SSA. The temporal evolution of these descriptors reported here provides new experimental data to develop and evaluate such parameterizations. As a first step toward developing physically based grain-shape descriptors, we investigated two curvature-based descriptors. Additional shape descriptors could be explored using the dataset of

https://doi.org/10.5194/egusphere-2026-4897
Preprint. Discussion started: 31 August 2026

Dick et al. (2026b) to address specific application needs. The implications for SSA and structural anisotropy modeling are discussed in dedicated sections below.

Beyond predicting a small set of scalar descriptors, future snowpack models could benefit from predicting the full chord length and mean curvature distributions, from which application-specific descriptors could be derived.

Modeling SSA

Current snowpack models assume that SSA decreases monotonically during dry snow metamorphism (Brun et al., 1992; Lehning et al., 2002; Vionnet et al., 2012). However, Wang and Baker (2014) and the present study show that this assumption is not always appropriate during TGM, as a wide range of SSA evolutions are observed, including increases. Although the observed increases are modest, they are sufficient to modify the optical properties of snow and may therefore influence the surface energy budget (e.g., Warren, 1982; Flanner and Zender, 2006; Libois et al., 2013). For example, an increase in SSA from 20 to 25 m^2 kg^{-1} corresponds to a decrease of approximately 20% in optical diameter. Future SSA evolution laws should therefore be improved to reproduce the full range of SSA evolution observed during dry snow metamorphism.

In that direction, efforts have been made to propose physically based laws governing SSA evolution. In particular, Krol and Löwe (2018) derived an equation linking SSA evolution to the mean curvature and the normal interface growth velocity. These two fields are defined for smooth surfaces evolving continuously in time. Our experiments show that significant topological changes can happen under certain metamorphism scenarios, as large genus variations are obtained. These topological changes produce singularities in the mean curvature and velocity fields, which need to be carefully taken into account when using this equation. More recently, Braun et al. (2024) suggested a linear relation between σ_H^2 and $(\rho_{ice}\,\mathrm{SSA})^2$. We evaluated this relationship using our dataset and found that it holds only for a limited subset of the experiments, mainly for the DF samples and for temperature gradients up to 40 K m^{-1} (Appendix, Fig. A4). This suggests that the proposed relationship is not yet sufficiently general for the range of snow types and metamorphism conditions investigated here.

More generally, our dataset indicates that SSA evolution laws should account for snow microstructure, mean temperature, and temperature gradient. In particular, the initial SSA alone does not appear to be sufficient to characterize the influence of the snow microstructure, as shown in Sect. 4.1. Another controlling factor under ETM might be the mean curvature variance, as suggested by Braun et al. (2024). Consequently, evolution laws such as that of Taillandier et al. (2007), which depend only on the initial SSA and mean temperature, are unlikely to capture the full diversity of SSA evolution during dry snow metamorphism.

Modeling structural anisotropy

Structural anisotropy controls the anisotropy of several physical and mechanical properties of snow (e.g., Leinss et al., 2016; Sundu et al., 2024). For example, the thermal conductivity of vertically oriented depth hoar can be up to 1.5 times greater in the vertical direction than in the horizontal plane (Calonne et al., 2011). Despite this,

https://doi.org/10.5194/egusphere-2026-4897
Preprint. Discussion started: 31 August 2026

structural anisotropy is not yet represented in operational snowpack models, although a first parameterization was recently proposed by Leinss et al. (2020). In this formulation, temperature-gradient metamorphism systematically drives the ice structure toward a more vertically oriented configuration, with the rate of evolution depending on the applied temperature gradient and the initial anisotropy.

Our observations do not support this predicted systematic increase in vertical anisotropy. Under weak and moderate temperature gradients, the snow microstructure may instead evolve toward a more horizontally oriented configuration. A direct comparison between the predictions of Leinss et al. (2020) and our observations is provided in Fig. 12. Our results indicate that the temperature gradient, the mean temperature, and the initial structural anisotropy should all be accounted for when modeling the evolution of structural anisotropy. However, the way these factors are represented in the parameterization of Leinss et al. (2020) should be refined, as it does not capture the diversity of the observed anisotropy evolution. Furthermore, our results suggest that the evolution may also depend on additional characteristics of the initial snow microstructure, such as density.

5 Conclusion

We investigated the temporal evolution of different grain-size and grain-shape descriptors during 20 experiments of equi-temperature and temperature-gradient metamorphism. Seven scalar descriptors were analyzed: SSA and its derived optical diameter, correlation length, microwave grain size, structural anisotropy, and three curvature-based shape descriptors. Furthermore, the temporal evolution of the chord length and mean curvature distributions was characterized. The respective influences of the temperature gradient, the mean temperature, and the initial snow microstructure on the grain size and shape evolution were highlighted.

Our main conclusions are:

1. Increasing the temperature gradient generally accelerates the evolution of snow microstructure descriptors, whereas decreasing the mean temperature slows it down. However, several descriptors exhibit behaviors that depart from these general trends.

2. The initial snow microstructure strongly controls grain-shape evolution and, to a lesser extent, grain-size evolution. In particular, snow with high initial SSA (around 60 m^2 kg^{-1}) exhibits more systematic and monotonic evolution during both TGM and ETM than rounded grains do.

3. SSA may either decrease or increase during TGM depending on the initial snow microstructure and the applied temperature gradient. This contrasts with the monotonic decrease generally assumed in snowpack models.

4. Correlation length and microwave grain size consistently increase during both ETM and TGM, whereas the optical diameter may increase, decrease, or remain nearly constant. They are also about two to three times smaller than the optical diameter throughout the experiments. Thus, choosing the grain-size descriptor appropriate to the physical process under investigation is particularly important.

https://doi.org/10.5194/egusphere-2026-4897
Preprint. Discussion started: 31 August 2026

5. The development of vertical ice orientation is not systematic during TGM, as horizontal orientation may instead be reinforced depending on the applied temperature gradient and the initial anisotropy.

This study provides new perspectives for improving snowpack models regarding the choice of microstructural descriptors and the formulation of their evolution laws. In particular, current SSA evolution laws in snowpack models could be refined using the experimental observations presented here. Snowpack models could also benefit from representing multiple complementary descriptors of grain size and grain shape. For example, models could predict the optical diameter for optical applications together with the microwave grain size or the correlation length for microwave applications. Grain shape could be represented using curvature-based descriptors, such as the mean curvature variance or the Willmore energy, as explored in this study. An even richer representation of snow microstructure could be achieved by predicting the full chord length and mean curvature distributions, from which multiple application-specific descriptors can be derived.

Although this study covers a wide range of snow types and metamorphism conditions, future work could extend the dataset to additional snow types, such as precipitation particles and melt forms, and thereby further support the development of next-generation snowpack models.

Data availability. Data presented in this paper are available on Zenodo at the temporary link https://zenodo.org/records/21807198?preview=1&token=eyJhbGciOiJIUzUxMiJ9.eyJpZCI6IjUxMGMyODk3LWMwZTEtNDQwNC05YTc4LWQ2NjgxMTQ2MjRlMCIsImRhdGEiOnt9LCJyYW5kb20iOiI3YzNjODRiZjFmNGY5NGZhOWNjMjRiMzI0NzQ0Yjk4ZCJ9.pDsRMRUmjudI4Gej6B1b2V0_p4RVrI9SHqZs5202gQUSqdwl8v9PukJ2Bcca0Ff3jJWiE5tX8_l86jDx9_VbVQ. Data will be made permanently available on Zenodo once the present work has been reviewed.

https://doi.org/10.5194/egusphere-2026-4897
Preprint. Discussion started: 31 August 2026

Author contributions. OD, PH, and NC designed the study. OD ran the numerical computations. OD wrote the paper with help from NC and contributions from PH.

Competing interests. The authors declare that no competing interests are present.

Acknowledgements. The tomography apparatus (TomoCold) was funded by INSU-LEFE, Labex OSUG (Investissements d'avenir, grant ANR-10-LABX-0056), and the CNRM. CNRM/CEN is part of Labex OSUG@2020 (Investissements d'Avenir, grant ANR-10-LABX-0056). This research has been supported by the European Research Council (ERC) StG IVORI project (European Union's Horizon 2020 research and innovation program grant no. 949516).

https://doi.org/10.5194/egusphere-2026-4897
Preprint. Discussion started: 31 August 2026

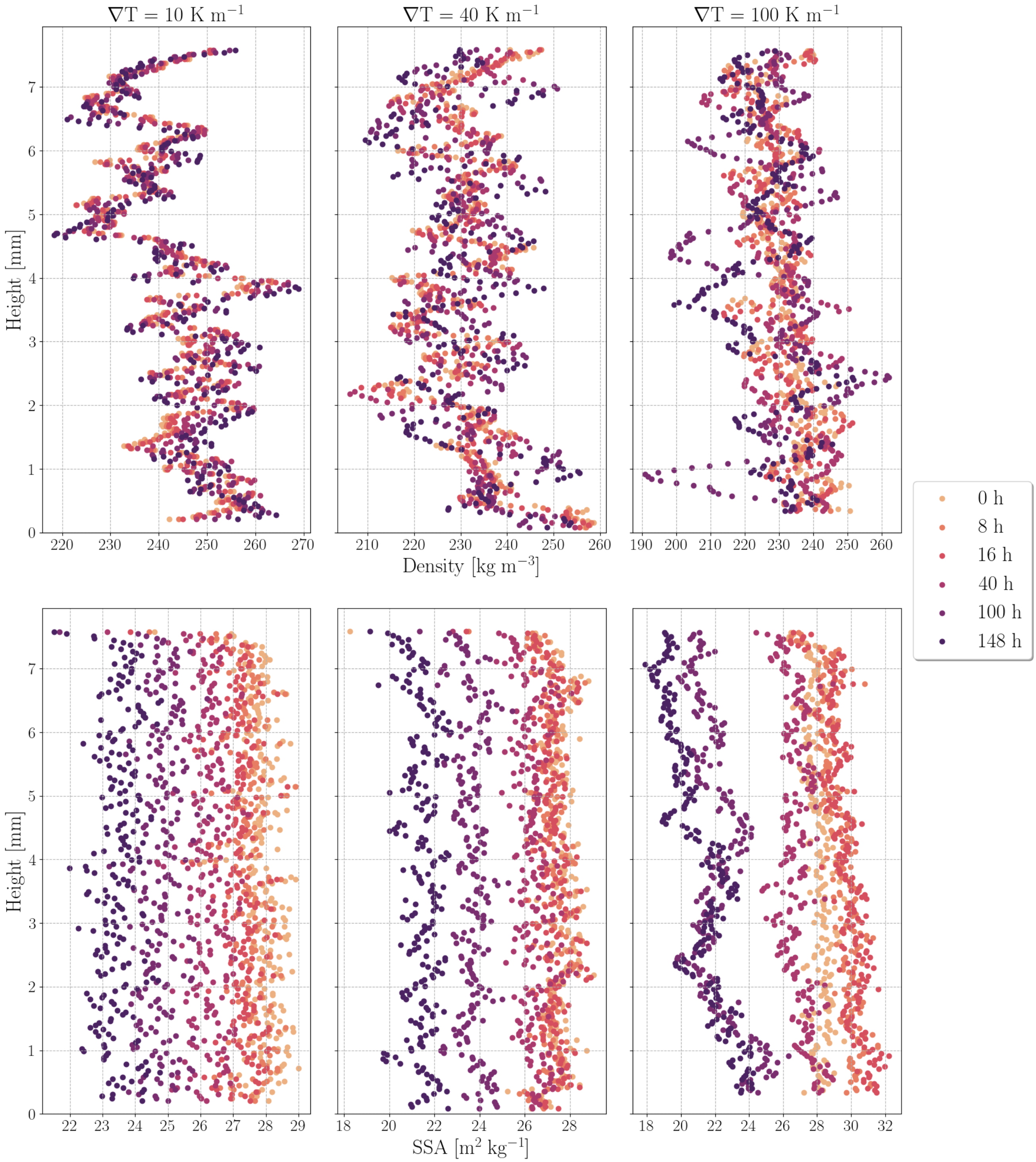

Figure A1. Density and SSA vertical profiles at six time steps for RGl samples exposed to gradients of 10, 40 and 100 K m^{-1} at -3°C. For these three experiments, the bottom ice layer was cropped from the image: a maximum of 0.34 mm was removed for the gradient of 100 K m^{-1}.

https://doi.org/10.5194/egusphere-2026-4897
Preprint. Discussion started: 31 August 2026

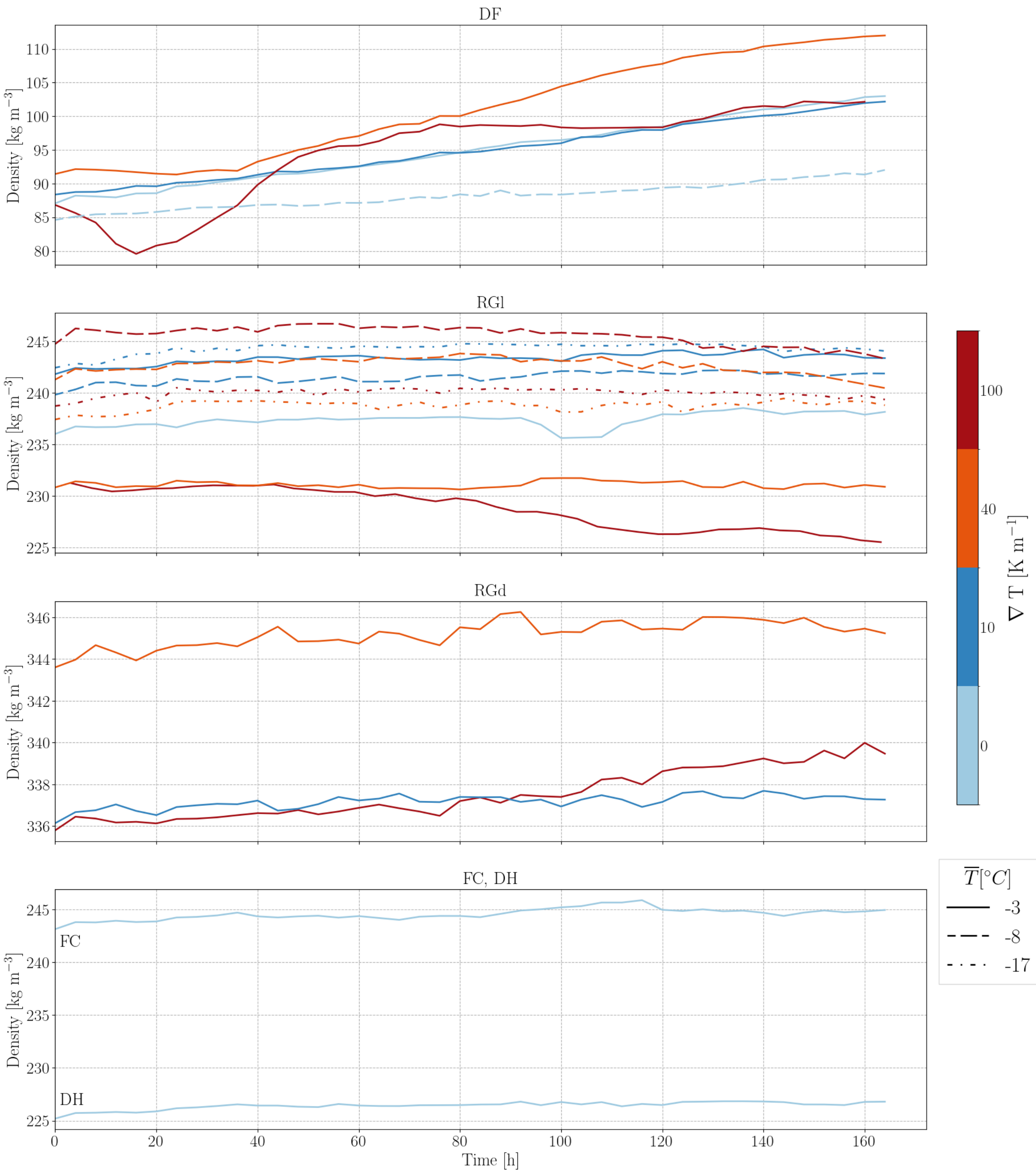

Figure A2. Evolution of density for DF, RGl, FC and DH samples during the TGM and ETM experiments.

https://doi.org/10.5194/egusphere-2026-4897
Preprint. Discussion started: 31 August 2026

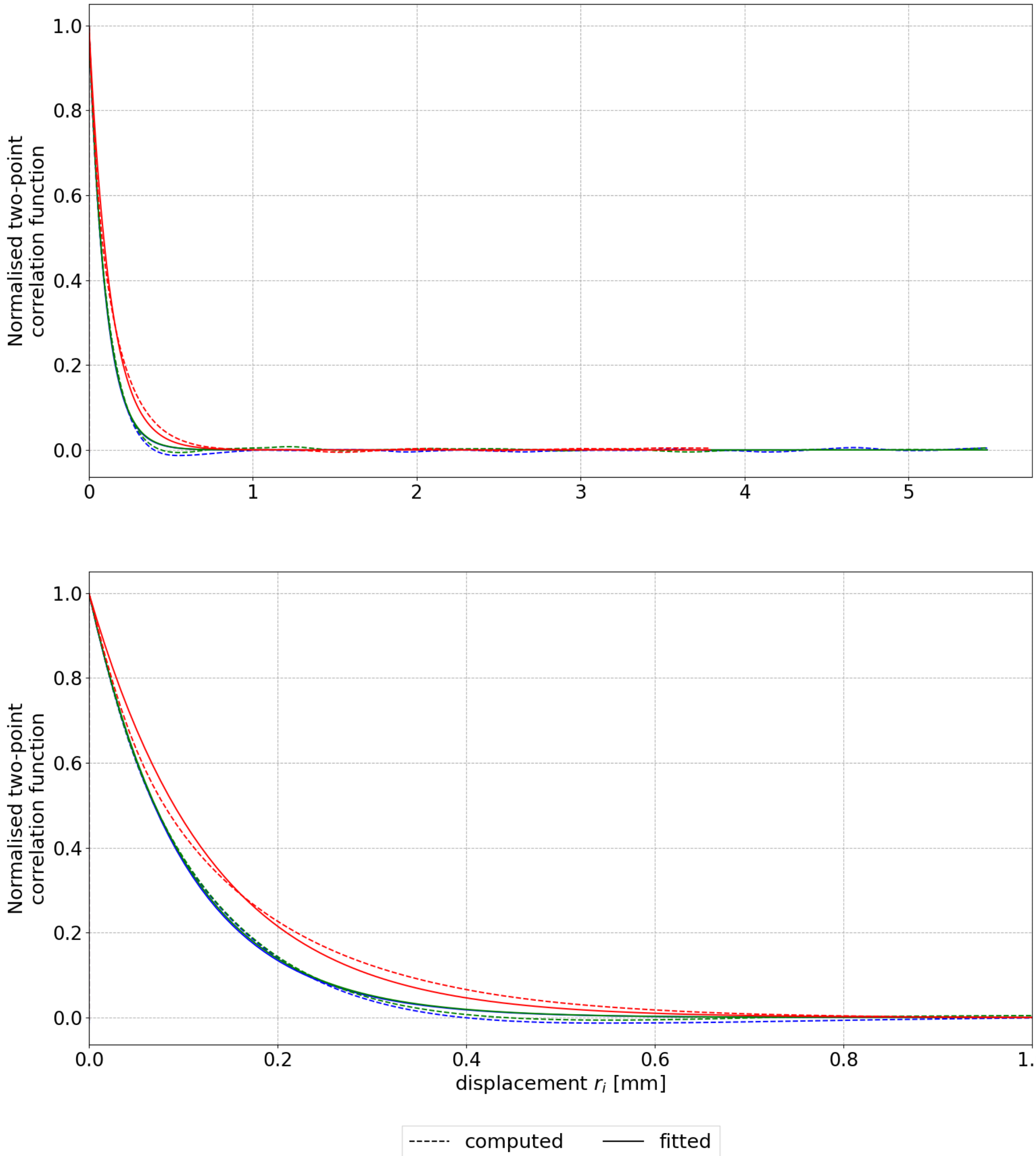

Figure A3. Normalized two-point correlation function for the whole range of displacement r_i above and magnified below for a sample of depth hoar. Dashed lines correspond to the two-point correlation function defined in Eq.6 in the x (blue), y (green), and z directions (red), while solid lines correspond to their respective exponential fits computed from Eq.7.

https://doi.org/10.5194/egusphere-2026-4897
Preprint. Discussion started: 31 August 2026

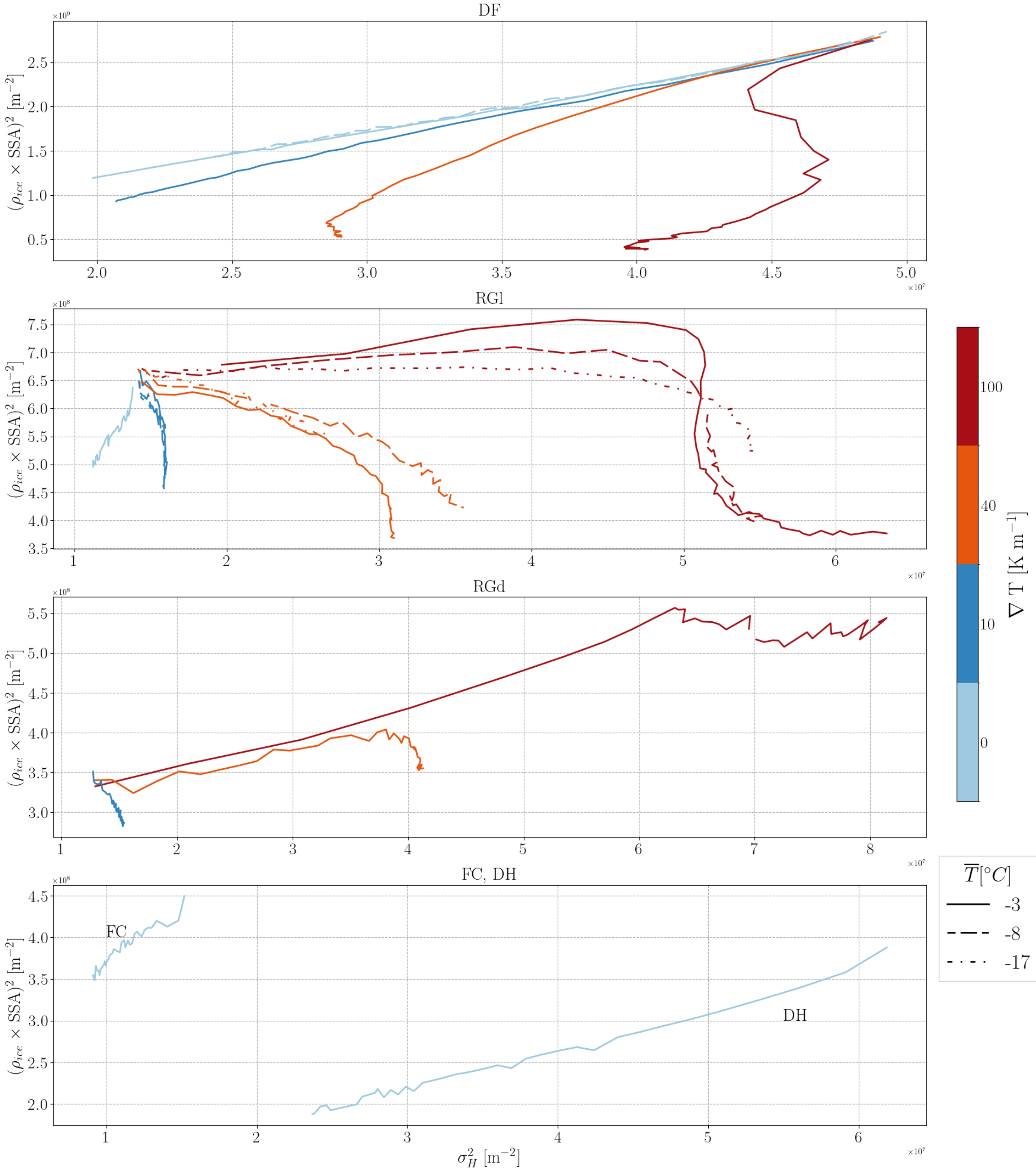

Figure A4. Evolution of $(\rho_{ice}\,\mathrm{SSA})^2$ against σ_H^2 for DF, RGl, FC, and DH samples during the TGM and ETM experiments.

https://doi.org/10.5194/egusphere-2026-4897
Preprint. Discussion started: 31 August 2026

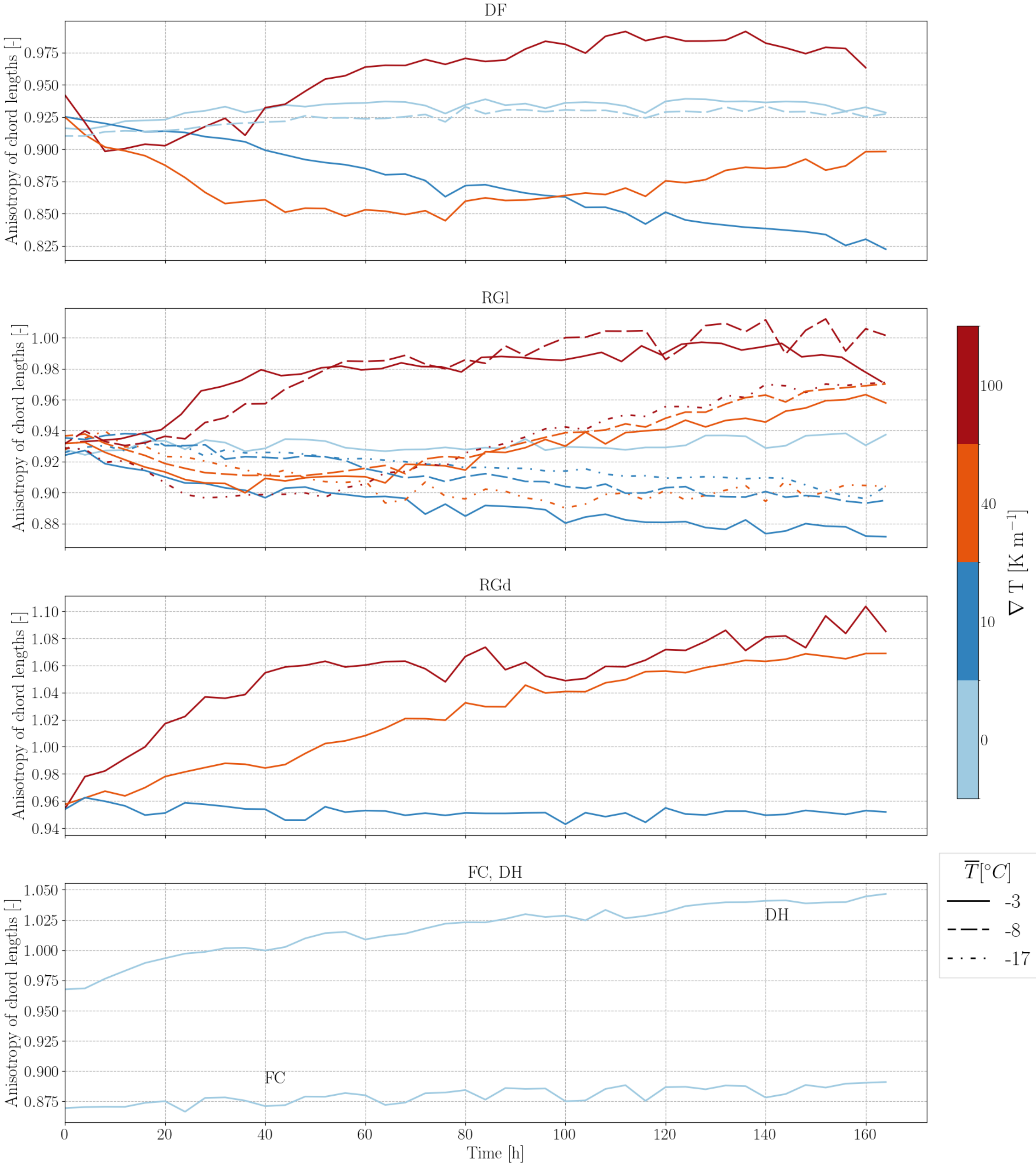

Figure A5. Evolution of the anisotropy ratio based on the mean chord lengths for DF, RGl, FC and DH samples during the TGM and ETM experiments.

https://doi.org/10.5194/egusphere-2026-4897
Preprint. Discussion started: 31 August 2026

References

Arakawa, H., Izumi, K., Kawashima, K., and Kawamura, T.: Study on quantitative classification of seasonal snow using specific surface area and intrinsic permeability, Cold. Reg. Sci. Technol., 59, 163–168, https://doi.org/10.1016/j.coldregions.2009.07.004, 2009.

Barrere, M., Domine, F., Decharme, B., Morin, S., Vionnet, V., and Lafaysse, M.: Evaluating the performance of coupled snow–soil models in SURFEXv8 to simulate the permafrost thermal regime at a high Arctic site., Geoscientific Model Development, 10, 2017.

Bernard, A., Hagenmuller, P., Montagnat, M., and Chambon, G.: Disentangling creep and isothermal metamorphism during snow settlement with X-ray tomography, Journal of Glaciology, 69, 899–910, 2023.

Bouvet, L., Calonne, N., Flin, F., and Geindreau, C.: Snow Equi-Temperature Metamorphism Described by a Phase-Field Model Applicable on Micro-Tomographic Images: Prediction of Microstructural and Transport Properties, Journal of Advances in Modeling Earth Systems, 14, e2022MS002 998, 2022.

Bouvet, L., Calonne, N., Flin, F., and Geindreau, C.: Heterogeneous grain growth and vertical mass transfer within a snow layer under a temperature gradient, The Cryosphere, 17, 3553–3573, 2023.

Boykov and Kolmogorov: Computing geodesics and minimal surfaces via graph cuts, in: Proceedings Ninth IEEE international conference on computer vision, pp. 26–33, IEEE, 2003.

Braun, A., Fourteau, K., and Löwe, H.: A rigorous approach to the specific surface area evolution in snow during temperature gradient metamorphism, The Cryosphere, 18, 1653–1668, https://doi.org/10.5194/tc-18-1653-2024, publisher: Copernicus GmbH, 2024.

Brun, E., David, P., Sudul, M., and Brunot, G.: A numerical model to simulate snow-cover stratigraphy for operational avalanche forecasting, J. Glaciol., 38, 13 – 22, 1992.

Brzoska, J.-B., Flin, F., and Barckicke, J.: Explicit iterative computation of diffusive vapour field in the 3-D snow matrix: preliminary results for low flux metamorphism, Ann. Glaciol., 48, 13–18, https://doi.org/10.3189/172756408784700798, 2008.

Cabanes, A., Legagneux, L., and Dominé, F.: Rate of evolution of the specific surface area of surface snow layers, Environ. Sci. Technol., 37, 661–666, 2003.

Calonne, N., Richter, B., Löwe, H., Cetti, C., ter Schure, J., Van Herwijnen, A., Fierz, C., Jaggi, M., and Schneebeli, M.: The RHOSSA campaign: multi-resolution monitoring of the seasonal evolution of the structure and mechanical stability of an alpine snowpack, The Cryosphere, 14, 1829–1848, https://doi.org/10.5194/tc-14-1829-2020, 2020.

Calonne, N.: Physique des métamorphoses de la neige sèche : de la microstructure aux propriétés macroscopiques, Ph.D. thesis, Université de Grenoble, 2014.

Calonne, N., Flin, F., Morin, S., Lesaffre, B., du Roscoat, S. R., and Geindreau, C.: Numerical and experimental investigations of the effective thermal conductivity of snow, Geophysical Research Letters, 38, L23 501, https://doi.org/10.1029/2011GL049234, 2011.

Calonne, N., Geindreau, C., Flin, F., Morin, S., Lesaffre, B., Rolland du Roscoat, S., and Charrier, P.: 3-D image-based numerical computations of snow permeability: links to specific surface area, density, and microstructural anisotropy, The Cryosphere, 6, 939–951, https://doi.org/10.5194/tc-6-939-2012, 2012.

Calonne, N., Flin, F., Geindreau, C., Lesaffre, B., and Rolland du Roscoat, S.: Study of a temperature gradient metamorphism of snow from 3-D images: time evolution of microstructures, physical properties and their associated anisotropy, The Cryosphere, 8, 2255–2274, https://doi.org/10.5194/tc-8-2255-2014, 2014a.

Calonne, N., Geindreau, C., and Flin, F.: Macroscopic modeling for heat and water vapor transfer in dry snow by homogenization, The Journal of Physical Chemistry B, 118, 13 393–13 403, https://doi.org/10.1021/jp5052535, 2014b.

Colbeck, S., Akitaya, E., Armstrong, R., Gubler, H., Lafeuille, J., Lied, K., McClung, D., and Morris, E.: The International classification for seasonal snow on the ground, International Commission on Snow and Ice of the International Association of Scientific Hydrology, World Data Center A for Glaciology, University of Colorado, Boulder, 1990.

Colbeck, S. C.: Theory of metamorphism of dry snow, J. Geophys. Res., 88, 5475–5482, (10.1029/0JGREA0000880000C9005475000001), 1983.

Coléou, C., Lesaffre, B., Brzoska, J.-B., Ludwig, W., and Boller, E.: Three-dimensional snow images by X-ray microtomography, Ann. Glaciol., 32, 75–81, https://doi.org/10.3189/172756401781819418, 2001.

Debye, P., Anderson, H. R., and Brumberger, H.: Scattering by an inhomogeneous solid II. The correlation function and its applications, J. Appl. Phys., 28, 679–683, 1957.

DGtal: DGtal: Digital Geometry tools and algorithms library, http://dgtal.org.

Dick, O., Calonne, N., Hagenmuller, P., and Laurent, B.: Time series and videos of 3D snow images: 20 scenarios of dry snow metamorphism monitored by X-ray tomography [dataset], PANGAEA, https://doi.org/https://doi.org/10.1594/PANGAEA.992556, 2026a.

Dick, O., Calonne, N., Laurent, B., and Hagenmuller, P.: Monitoring dry snow metamorphism using 4D tomography across 20 experimental conditions, Earth System Science Data Discussions, 2026, 1–23, 2026b.

Domine, F., Taillandier, A.-S., Cabanes, A., Douglas, T., and Sturm, M.: Three examples where the specific surface area of snow increased over time, The Cryosphere, 3, 31–39, 2009.

Domine, F., Picard, G., Morin, S., Barrere, M., Madore, J.-B., and Langlois, A.: Major issues in simulating some Arctic snowpack properties using current detailed snow physics models: Consequences for the thermal regime and water budget of permafrost, Journal of Advances in Modeling Earth Systems, 11, 34–44, 2019.

Dumont, M., Brun, E., Picard, G., Michou, M., Libois, Q., Petit, J., Geyer, M., Morin, S., and Josse, B.: Contribution of light-absorbing impurities in snow to Greenland's darkening since 2009, Nature Geoscience, 7, 509–512, 2014.

Dumont, M., Laurent, A., Picard, G., Libois, Q., Lejeune, Y., Nabat, P., Voisin, D., and Morin, S.: In situ continuous visible and near-infrared spectroscopy of an alpine snowpack, The Cryosphere, 11, 1091, 2017.

Fierz, C., Armstrong, R. L., Durand, Y., Etchevers, P., Greene, E., McClung, D. M., Nishimura, K., Satyawali, P. K., and Sokratov, S. A.: The international classification for seasonal snow on the ground, IHP-VII Technical Documents in Hydrology n 83, IACS Contribution n 1, 2009.

Flanner, M. G. and Zender, C. S.: Linking snowpack microphysics and albedo evolution, J. Geophys. Res., 111, D12 208, https://doi.org/10.1029/2005JD006834, 2006.

Flin, F., Brzoska, J.-B., Lesaffre, B., Coléou, C., and Pieritz, R. A.: Full three-dimensional modelling of curvature-dependent snow metamorphism: first results and comparison with experimental tomographic data, J. Phys. D: Appl. Phys., 36, A49–A54, https://doi.org/10.1088/0022-3727/36/10A/310, 2003.

https://doi.org/10.5194/egusphere-2026-4897
Preprint. Discussion started: 31 August 2026

Flin, F., Brzoska, J. B., Lesaffre, B., Coleou, C., and Pieritz, R. A.: Three-dimensional geometric measurements of snow microstructural evolution under isothermal conditions, Annals of glaciology, 38, 39–44, 2004.

Gardner, A. S. and Sharp, M.: A review of snow and ice albedo and the development of a new physically based broadband albedo parametrization, J. Geophys. Res., 115, F01 009, https://doi.org/10.1029/2009JF001444, 2010.

Grenfell, T. C., Warren, S. G., and Mullen, P. C.: Reflection of solar radiation by the Antarctic snow surface at ultaviolet, visible, and near-infrared wavelengths, J. Geophys. Res., 99, 18,669 – 18,684, 1994.

Hachikubo, A., Yamaguchi, S., Arakawa, H., Tanikawa, T., Hori, M., Sugiura, K., Matoba, S., Niwano, M., Kuchiki, K., and Aoki, T.: Effects of temperature and grain type on time variation of snow specific surface area, Bulletin of Glaciological Research, 32, 47–53, 2014.

Hadwiger, H.: Vorlesungen tiber inhalt, oberflache und isoperimetrie, in: Vorlesungen tiber Inhalt, Oberflache und Isoperimetrie, pp. 179–198, Springer, 1957.

Hagenmuller, P., Theile, T. C., and Schneebeli, M.: Numerical simulation of microstructural damage and tensile strength of snow, Geophysical Research Letters, 41, 86–89, 2014.

Hagenmuller, P., Matzl, M., Chambon, G., and Schneebeli, M.: Sensitivity of snow density and specific surface area measured by microtomography to different image processing algorithms, The Cryosphere, 10, 1039–1054, 2016.

Ho, F. G. and Strieder, W.: Asymptotic expansion of the porous medium, effective diffusion coefficient in the Knudsen number, The Journal of Chemical Physics, 70, 5635–5639, 1979.

Holko, L., Gorbachova, L., and Kostka, Z.: Snow hydrology in central Europe, Geography Compass, 5, 200–218, 2011.

Kaempfer, T., Schneebeli, M., and Sokratov, S.: A microstructural approach to model heat transfer in snow, Geophys. Res. Lett., 32, L21 503, https://doi.org/10.1029/2005GL023873, 2005.

Kaempfer, T. U. and Schneebeli, M.: Observation of isothermal metamorphism of new snow and interpretation as a sintering process, Journal of Geophysical Research: Atmospheres, 112, 2007.

Krol, Q. and Löwe, H.: Relating optical and microwave grain metrics of snow: The relevance of grain shape, The Cryosphere Discusssion, https://doi.org/doi:10.5194/tc-2016-119, 2016.

Krol, Q. and Löwe, H.: Upscaling ice crystal growth dynamics in snow: Rigorous modeling and comparison to 4D X-ray tomography data, Acta Materialia, 151, 478–487, 2018.

Lachaud, J.-O., Romon, P., and Thibert, B.: Corrected Curvature Measures, Discrete and Computational Geometry, 68, 477–524, https://doi.org/10.1007/s00454-022-00399-4, 2022.

Lafaysse, M., Dumont, M., De Fleurian, B., Fructus, M., Nheili, R., Viallon-Galinier, L., Baron, M., Boone, A., Bouchet, A., Brondex, J., et al.: Version 3.0 of the Crocus snowpack model, EGUsphere, 2025, 1–75, 2025.

Legagneux, L. and Dominé, F.: A mean field model of the decrease of the specific surface area of dry snow during isothermal metamorphism, J. Geophys. Res., 110, F04 011, https://doi.org/10.1029/2004JF000181, 2005.

Legagneux, L., Taillandier, A.-S., and Domine, F.: Grain growth theories and the isothermal evolution of the specific surface area of snow, J. Appl. Phys., 95, 6175–6184, 2004.

Lehmann, G. and Legland, D.: Efficient N-dimensional surface estimation using Crofton formula and run-length encoding, Efficient N-Dimensional surface estimation using Crofton formula and run-length encoding, Kitware INC (2012), 2012.

https://doi.org/10.5194/egusphere-2026-4897
Preprint. Discussion started: 31 August 2026

Lehning, M., Bartelt, P., Brown, B., Fierz, C., and Satyawali, P.: A physical SNOWPACK model for the Swiss avalanche warning. Part II: snow microstructure., Cold Reg. Sci. Technol., 35, 147 – 167, https://doi.org/10.1016/S0165-232X(02)00073-3, 2002.

Leinss, S., Löwe, H., Proksch, M., Lemmetyinen, J., Wiesmann, A., and Hajnsek, I.: Anisotropy of seasonal snow measured by polarimetric phase differences in radar time series, The Cryosphere, 10, 1771–1797, 2016.

Leinss, S., Löwe, H., Proksch, M., and Kontu, A.: Modeling the evolution of the structural anisotropy of snow, The Cryosphere, 14, 51–75, 2020.

Libois, Q., Picard, G., France, J., Arnaud, L., Dumont, M., Carmagnola, C. M., and King, M.: Influence of grain shape on light penetration in snow, The Cryosphere, 7, 1803–1818, https://doi.org/10.5194/tc-7-1803-2013, 2013.

Löwe, H., Riche, F., and Schneebeli, M.: A general treatment of snow microstructure exemplified by an improved relation for thermal conductivity, The Cryosphere, 7, 1473–1480, https://doi.org/10.5194/tc-7-1473-2013, 2013.

Malinka, A. V.: Light scattering in porous materials: Geometrical optics and stereological approach, Journal of Quantitative Spectroscopy and Radiative Transfer, 141, 14–23, 2014.

Mätzler, C.: Relation between grain-size and correlation length of snow, Journal of Glaciology, 48, 461–466, 2002.

Méring, J. and Tchoubar, D.: Interprétation de la diffusion centrale des rayons X par les systemes poreux. I, Applied Crystallography, 1, 153–165, 1968.

Morin, S., Domine, F., Dufour, A., Lejeune, Y., Lesaffre, B., Willemet, J.-M., Carmagnola, C. M., and Jacobi, H.-W.: Measurements and modeling of the vertical profile of specific surface area of an alpine snowpack, Adv. Water Res., 55, 111–120, https://doi.org/10.1016/j.advwatres.2012.01.010, 2013.

Mullins, W. W. and Sekerka, R.: Stability of a planar interface during solidification of a dilute binary alloy, Journal of applied physics, 35, 444–451, 1964.

Newman, M. E. and Barkema, G. T.: Monte Carlo methods in statistical physics, Clarendon Press, 1999.

Picard, G., Löwe, H., Domine, F., Arnaud, L., Larue, F., Favier, V., Le Meur, E., Lefebvre, E., Savarino, J., and Royer, A.: The Microwave Snow Grain Size: A New Concept to Predict Satellite Observations Over Snow-Covered Regions, AGU Advances, 3, e2021AV000 630, https://doi.org/https://doi.org/10.1029/2021AV000630, e2021AV000630 2021AV000630, 2022.

Pinkall, U. and Gross, O.: Willmore surfaces, in: Differential Geometry: From Elastic Curves to Willmore Surfaces, pp. 181–191, Springer, 2024.

Richeson, D. S.: Euler's gem: the polyhedron formula and the birth of topology, vol. 41, Princeton University Press, 2010.

Schleef, S. and Loewe, H.: X-ray microtomography analysis of isothermal densification of new snow under external mechanical stress, J. Glaciol., 59, 214, https://doi.org/doi:10.3189/2013JoG12J076, 2013.

Schleef, S., Jaggi, M., Löwe, H., and Schneebeli, M.: Instruments and methods: An improved machine to produce nature-identical snow in the laboratory, Journal of Glaciology, 60, 94–102, https://doi.org/10.3189/2014JoG13J118, 2014a.

Schleef, S., Jaggi, M., Löwe, H., and Schneebeli, M.: An improved machine to produce nature-identical snow in the laboratory, Journal of Glaciology, 60, 94–102, 2014b.

Schleef, S., Löwe, H., and Schneebeli, M.: Hot-pressure sintering of low-density snow analyzed by X-ray microtomography and in situ microcompression, Acta Materialia, 71, 185–194, https://doi.org/10.1016/j.actamat.2014.03.004, 2014c.

Schneebeli, M. and Sokratov, S. A.: Tomography of temperature gradient metamorphism of snow and associated changes in heat conductivity, Hydrol. Process., 18, 3655 – 3665, https://doi.org/10.1002/hyp.5800, 2004.

https://doi.org/10.5194/egusphere-2026-4897
Preprint. Discussion started: 31 August 2026

Schweizer, J., Jamieson, J. B., and Schneebeli, M.: Snow avalanche formation, Reviews of Geophysics, 41, 2003.

Sundu, K., Freitag, J., Fourteau, K., and Löwe, H.: A microstructure-based parameterization of the effective anisotropic elasticity tensor of snow, firn, and bubbly ice, The Cryosphere, 18, 1579–1596, 2024.

Taillandier, A.-S., Domine, Simpson, W. R., Sturm, M., and Douglas, T. A.: Rate of decrease of the specific surface area of dry snow: Isothermal and temperature gradient conditions, J. Geophys. Res., 112, F03 003, https://doi.org/10.1029/2006JF000514, 2007.

Tassopoulos, M. and Rosner, D. E.: Simulation of vapor diffusion in anisotropic particulate deposits, Chemical engineering science, 47, 421–443, 1992.

Torquato, S.: Random Heterogeneous Materials: Microstructure and Macroscopic Properties, Springer-Verlag, New York, 2002.

Underwood, E.: Stereology, or the quantitative evaluation of microstructures, Journal of microscopy, 89, 161–180, 1969.

Vallese, F. and Kong, J.: Correlation function studies for snow and ice, Journal of Applied Physics, 52, 4921–4925, 1981.

Vionnet, V., Brun, E., Morin, S., Boone, A., Martin, E., Faroux, S., Moigne, P. L., and Willemet, J.-M.: The detailed snowpack scheme Crocus and its implementation in SURFEX v7.2, Geosci. Model. Dev., 5, 773–791, https://doi.org/10.5194/gmd-5-773-2012, 2012.

Wang, X. and Baker, I.: Evolution of the specific surface area of snow during high-temperature gradient metamorphism, Journal of Geophysical Research: Atmospheres, 119, 13–690, 2014.

Warren, S.: Optical properties of snow, Rev. Geophys., 20, 67–89, https://doi.org/10.1029/RG020i001p00067, 1982.

Wiese, M. and Schneebeli, M.: Early-stage interaction between settlement and temperature-gradient metamorphism, Journal of Glaciology, 63, 652–662, 2017.

Wiesmann, A. and Mätzler, C.: Microwave emission model of layered snowpacks, Remote sensing of environment, 70, 307–316, 1999.

Willmore, T. J.: A survey on Willmore immersions, Geometry and topology of submanifolds, IV (Leuven, 1991), pp. 11–16, 1992.

Wiscombe, W. J. and Warren, S. G.: A model for the spectral albedo of snow. I: Pure snow, J. Atmos. Sci., 37(12), 2712 – 2733, 1980.

Woolley, G. J., Rutter, N., Wake, L., Vionnet, V., Derksen, C., Essery, R., Marsh, P., Tutton, R., Walker, B., Lafaysse, M., et al.: Multi-physics ensemble modelling of Arctic tundra snowpack properties, The Cryosphere, 18, 5685–5711, 2024.

Woolley, G. J., Rutter, N., Wake, L., Vionnet, V., Derksen, C., Meloche, J., Montpetit, B., Leroux, N. R., Essery, R., Hould Gosselin, G., et al.: Simulating snow properties and Ku-band backscatter across the forest-tundra ecotone, The Cryosphere, 20, 1315–1338, 2026.

Yosida, Z., Oura, H., Kuroiwa, D., Huzioka, T., Kojima, K., Aoki, S., and Kinosita, S.: Physical Studies on Deposited Snow: I Thermal Properties, Tech. Rep. 7, Institute of Low Temperature Science, Hokkaido University, Sapporo, Japan, 1955.

Zermatten, E., Haussener, S., Schneebeli, M., and Steinfeld, A.: Tomography-based determination of permeability and Dupuit-Forchheimer coefficient of characteristic snow samples, J. Glaciol., 57, 811–816, https://doi.org/10.3189/002214311798043799, 2011.